Ultrafast Measurements of Mode-Specific Deformation Potentials of Bi_2Te_3 and Bi_2Se_3

Yijing Huang,[1,2,3,4,*] José D. Querales-Flores,[5] Samuel W. Teitelbaum,[2,6] Jiang Cao,[7] Thomas Henighan,[2,8] Hanzhe Liu,[2,8,9] Mason Jiang,[2,3] Gilberto De la Peña,[4,2] Viktor Krapivin,[2,3] Johann Haber,[2] Takahiro Sato,[10] Matthieu Chollet,[10] Diling Zhu,[10] Tetsuo Katayama,[11,12] Robert Power,[13] Meabh Allen,[13] Costel R. Rotundu,[4] Trevor P. Bailey,[14] Ctirad Uher,[14] Mariano Trigo,[2,4] Patrick S. Kirchmann,[4] Éamonn D. Murray,[15] Zhi-Xun Shen,[4,3] Ivana Savić,[16] Stephen Fahy,[13,5] Jonathan A. Sobota,[4,†] and David A. Reis[2,4,3,17,‡]

[1]*Department of Physics, University of Illinois at Urbana-Champaign, Urbana, Illinois 61801, USA*
[2]*Stanford PULSE Institute, SLAC National Accelerator Laboratory, Menlo Park, California 94025, USA*
[3]*Department of Applied Physics, Stanford University, Stanford, California 94305, USA*
[4]*Stanford Institute for Materials and Energy Sciences, SLAC National Accelerator Laboratory, Menlo Park, California 94025, USA*
[5]*Tyndall National Institute, Dyke Parade, Cork, Ireland*
[6]*Department of Physics, Arizona State University, Tempe, Arizona 85281, USA*
[7]*Integrated Systems Laboratory, ETH Zurich, Zürich, Switzerland*
[8]*Department of Physics, Stanford University, Stanford, California 94305, USA*
[9]*Department of Chemistry, Purdue University, West Lafayette, Indiana 47907, USA*
[10]*Linac Coherent Light Source, SLAC National Accelerator Laboratory, Menlo Park, California 94025, USA*
[11]*Japan Synchrotron Radiation Research Institute, Kouto 1-1-1, Sayo, Hyogo 679-5198, Japan*
[12]*RIKEN SPring-8 Center, 1-1-1 Kouto, Sayo, Hyogo 679-5148, Japan*
[13]*Department of Physics, University College Cork, College Road, Cork, Ireland*
[14]*Department of Physics, University of Michigan, Ann Arbor, Michigan 48109, USA*
[15]*Department of Physics and Department of Materials, Imperial College London, London SW7 2AZ, United Kingdom*
[16]*Department of Physics, King's College London, The Strand, London WC2R 2LS, United Kingdom*
[17]*Department of Photon Science, Stanford University, Stanford, California 94305, USA*

(Received 22 July 2023; revised 8 October 2023; accepted 15 November 2023; published 14 December 2023)

Quantifying electron-phonon interactions for the surface states of topological materials can provide key insights into surface-state transport, topological superconductivity, and potentially how to manipulate the surface state using a structural degree of freedom. We perform time-resolved x-ray diffraction (XRD) and angle-resolved photoemission (ARPES) measurements on Bi_2Te_3 and Bi_2Se_3, following the excitation of coherent A_{1g} optical phonons. We extract and compare the deformation potentials coupling the surface electronic states to local A_{1g}-like displacements in these two materials using the experimentally determined atomic displacements from XRD and electron band shifts from ARPES. We find the coupling in Bi_2Te_3 and Bi_2Se_3 to be similar and in general in agreement with expectations from density functional theory. We establish a methodology that quantifies the mode-specific electron-phonon coupling experimentally, allowing detailed comparison to theory. Our results shed light on fundamental processes in topological insulators involving electron-phonon coupling.

DOI: 10.1103/PhysRevX.13.041050

Subject Areas: Condensed Matter Physics, Materials Science

I. INTRODUCTION

Electron-phonon interactions are of fundamental importance in condensed matter. In the case of topological insulators the scattering properties of their topological surface states (SS) have a direct impact on their application to energy-efficient electronics [1–5]. Previous studies employed a variety of methods to study the electron-phonon coupling: self-energy analysis in angle-resolved photoemission (ARPES) [6–10], helium atom scattering [11,12], and

*huangyj@illinois.edu
†sobota@slac.stanford.edu
‡dreis@stanford.edu

transport measurements [13]. The metal-intercalated Bi_2Se_3 family of topological insulators are also topological superconductor candidates [14–18], where electron-phonon coupling potentially mediates unconventional pairing symmetries [19]. Therefore, quantifying the mode-specific electron-phonon coupling may benefit the search for and understanding of topological superconductors. Studying electron-phonon coupling is also beneficial for understanding and designing functional topological materials. For example, the SS has been predicted to facilitate certain chemical reactions [20,21], among which some benefit from phonon participation [22]. Finally, electron-phonon interactions hold implications for optical control of matter [23,24], for example, by ultrafast manipulation of SS transport [25], or by exciting certain lattice degrees of freedom to switch topological phases [26–29].

The deformation potential (DP) quantifies the electron-phonon coupling of a specific electronic band to a specific phonon mode as the change of electronic energy for a given lattice displacement [30]. Here, we report ultrafast measurements of band- and mode-specific DPs in the prototypical topological insulators Bi_2Te_3 and Bi_2Se_3. We measure the DPs of the SS coupled to A_{1g} phonons by combining the atomic displacements measured by XRD with the energy shift of the SS measured by time-resolved ARPES.

Before laying out our multimodal methodology in more detail, we provide a brief overview of other ARPES-based techniques used to quantify electron-phonon coupling. In equilibrium ARPES, electron-phonon coupling introduces kinks into the band dispersion which can be quantified via self-energy analysis to extract the dimensionless electron-phonon coupling constant λ [31]. This approach requires the assumption of a bare band dispersion and consideration of $\mathbf{q}$-dependent electron coupling [32]. For $\mathbf{q} \approx 0$ coupling, shakeoff bands may develop and together with theory λ can be estimated from their intensity ratios [33]. In time-resolved ARPES [34], electron-phonon coupling contributes to incoherent relaxation dynamics, characterized by nonoscillatory evolution of populations and spectral functions. This can be modeled by coupled heat baths of electrons and phonons [35] together with transport effects [36]. Individual modes are not resolved, and only the mode-weighted coupling λ is extracted [37]. More recently, discretized population dynamics due to scattering with strongly coupled high-energy phonons were observed [38], which permits mode assignment and calculation of the electron-phonon coupling matrix element. In general, for incoherent responses, care must be taken to avoid ambiguity between population relaxation times and single-particle lifetimes [39]. In time-resolved ARPES, electron-phonon coupling may also manifest as coherent oscillations in binding energies or intensities. This complements self-energy analysis in equilibrium by increased sensitivity to low-frequency modes and selectivity of only Raman-active modes near $\mathbf{q} = 0$. The amplitude of coherent electron-band oscillations by itself, however, only quantifies relative momentum- and band-dependent coupling strengths [40–42]. Quantitative extraction of mode-specific deformation potentials can be achieved with minimal modeling by combining shifts in the band energy obtained from time-resolved ARPES with shifts in atomic positions through time-resolved diffraction experiments following the sudden excitation of carriers and coherent phonons, as demonstrated by Refs. [43,44]. However, as we shall show in this work, additional quantitative uncertainties need to be considered due to different experimental conditions in ARPES and scattering experiments.

We find that the experimental DP of the $A_{1g}^{(1)}$ phonon mode is 1.4 times larger in Bi_2Te_3 than in Bi_2Se_3. Within experimental uncertainties the DPs are similar and on the order of 2 meV/pm. This qualitatively agrees with the naive expectation for two isostructural and isoelectronic materials and notably is a factor 5 smaller than in the strongly correlated superconductor FeSe [44]. Predictions from density functional theory (DFT) match experimental values within a factor of 2.5. DFT correctly predicts a larger DP in Bi_2Te_3 than in Bi_2Se_3. Constrained DFT calculations of the excited state reproduce the experimentally observed mode softening well. The consistent experimental values and their general agreement with theory validate our experimental and theoretical concepts while also pointing to their challenges. Our mode- and band-specific measurement of the DPs in prototypical topological insulators contributes to a microscopic understanding of SS transport where electron-phonon coupling is an important contribution to the scattering rates. The methodology we lay out could also be useful for the investigation of topological switches induced by structural change since one can monitor the structural change with XRD while observing the topological state with ARPES.

In the following, we define the DP with respect to A_{1g} modes and the SS in Bi_2Te_3 and Bi_2Se_3 as

$$\mathrm{DP} = \frac{\Delta E_{\mathrm{SS}}^{A_{1g}}}{u_{\mathrm{SS}}^{A_{1g}}}, \tag{1}$$

where $u_{\mathrm{SS}}^{A_{1g}}$ is an atomic displacement near the surface projected onto the bulk A_{1g} mode eigenvector [as shown in Fig. 1(a)] and averaged over the spatial extent of the SS. This definition allows us to formally define a surface deformation potential relative to a bulk phonon, even though the interatomic forces near the surface may be subtly different from true bulklike forces. $\Delta E_{\mathrm{SS}}^{A_{1g}}$ is the energy shift of the SS induced by the atomic displacement along the A_{1g} mode eigenvector. Below we choose to quantify $u_{\mathrm{SS}}^{A_{1g}}$ with respect to the bismuth displacements for

convenience in comparing the two materials. We suppress A_{1g} to simplify the notation in the following.

When combining XRD and ARPES data to calculate DPs, we need to account for the fact that the two methods are, respectively, bulk- and surface-sensitive probes. This is important because the finite penetration depth of the pump laser leads to diffusion of excited carriers and in turn to an inhomogeneous phonon displacement inside the probed volume of the sample. This can lead to systematic errors in the analysis that require correction depending on the experimental details. For example, the study in Gerber *et al.* [44] utilized FeSe films with a thickness comparable to the optical penetration depth; thus a quantitative correction due to diffusion is minor. In contrast, we require substantial corrections for the thicker Bi_2Te_3 and Bi_2Se_3 samples studied here.

The paper is organized as follows. First, we present the time-resolved ARPES and XRD experiments in Sec. II. We then detail the DP calculations in Sec. III, where, guided by simulations, we correct for methodological effects. In Sec. IV, we summarize the DFT calculations. In Sec. V we conclude our findings and suggest systematic improvements for future work.

II. EXPERIMENTAL DETAILS

In the XRD and ARPES experiments, Bi_2Se_3 and Bi_2Te_3 are pumped at room temperature with ultrafast 1.55 eV laser pulses. This excites fully symmetric coherent optical A_{1g} phonons that produce modulations in the XRD intensities from which we extract the amplitudes of phonon motions. The coherent A_{1g} phonons also induce electron band shifts via electron-phonon coupling, producing oscillations in electron band energies which we quantify using time-resolved ARPES.

We first describe the experiments on Bi_2Te_3. The atomic motion diagram in Fig. 1(a) shows the two A_{1g} modes. To extract the phonon amplitudes, we performed time-resolved XRD at the X-ray Pump-Probe (XPP) instrument of the Linac Coherent Light Source (LCLS) using 9.5 keV photon energy and a 50 nm Bi_2Te_3 film on sapphire. Both the optical laser and the x-ray laser are grazing incident on the sample in order to match their penetration depths. The time resolution is approximately 50 fs, taking into account the laser and x-ray pulse duration, after the correction of timing jitter between them. That is, the time resolution is given by the cross-correlation of the pump and the probe. Figure 1(b) shows the normalized time-dependent diffracted intensity $\Delta I/I$ of the (556) peak, which is sensitive to both $A_{1g}^{(1)}$ (1.8 THz) and $A_{1g}^{(2)}$ (3.9 THz) modes, as evidenced by the Fourier transform in Fig. 1(c). The A_{1g} phonons are launched through the displacive excitation of coherent phonons, where the quasiequilibrium phonon coordinates are suddenly shifted upon photoexcitation [45]. The photoexcited forces drive the phonon motion along [111] (see Appendix A for the rhombohedral primitive unit cell), illustrated with the purple ($A_{1g}^{(1)}$) and green ($A_{1g}^{(2)}$) arrows in Fig. 1(a). The time-dependent intensity modulations can be described as damped harmonic oscillators, each parametrized by an amplitude, a frequency, a damping constant, and an initial phase. We extract these parameters using a linear prediction singular value decomposition (LPSVD) method [46,47]. The initial phases of modes are approximately either 0 or π, subject to the uncertainty in time zero (which is approximately the quoted time resolution for each experiment). Using the method similar to Ref. [48], we are able to annotate the atomic motion as shown in Fig. 1(a). The fact that the initial phases of atomic displacements are approximately either 0 or π implies that the photoexcited electron density produces effectively instantaneous forces on atoms, which remain approximately constant over the considered time interval. This physically corresponds to sudden shifts in equilibrium atomic positions, which is compatible with the assumptions of our constrained DFT (CDFT) model (see below). The inset of Fig. 1(c) shows the fluence dependence of the normalized amplitude $\Delta I/I$. We constrain the linear fits (broken lines in the inset) to intersect the origin because the coherent atomic motion amplitude is zero without optical excitation. The intensity modulation amplitude is converted to vibrational mode amplitude using the phonon eigenvector experimentally determined by measuring multiple Bragg peaks (see Appendix A).

To extract the electron band energy shifts induced by coherent phonon motion, we performed time-resolved ARPES measurements on Bi_2Te_3 in our time-resolved ARPES laboratory. A single crystal of Bi_2Te_3 was cleaved in ultrahigh vacuum and probed using 6 eV UV laser with an overall time resolution of 60 fs, representing the cross-correlation between the near infrared (NIR) pump and UV probe pulses. The photoexcited ARPES spectrum at a delay time of 510 fs is shown in Fig. 1(d), with the SS (yellow) and conduction band (CB, red) denoted by the boxed regions. We fit the peak position of each energy distribution curve as a function of delay and parallel momentum $\mathbf{k}_{||}$ for the SS along Γ-K. We find negligible dependence on $\mathbf{k}_{||}$ (see Appendix B) and therefore average the time-resolved energy shifts over $\mathbf{k}_{||}$ within the indicated region to maximize the signal-to-noise ratio for the subsequent analysis. We note that the bulk states disperse in three dimensions, and there is substantial uncertainty in the probed out-of-plane momentum component $\mathbf{k}_{\perp}$, which precludes a quantitative analysis of the bulk bands [49]. In contrast, the SS has no $\mathbf{k}_{\perp}$ component and is therefore not subject to this ambiguity. Figure 1(e) shows the $\mathbf{k}_{||}$-averaged energy shifts of the SS as a function of fluence. The Fourier transform in Fig. 1(f) shows two main $A_{1g}^{(1)}$ and $A_{1g}^{(2)}$ peaks with shoulders associated with the surface termination [50,51]. The main peaks have the same

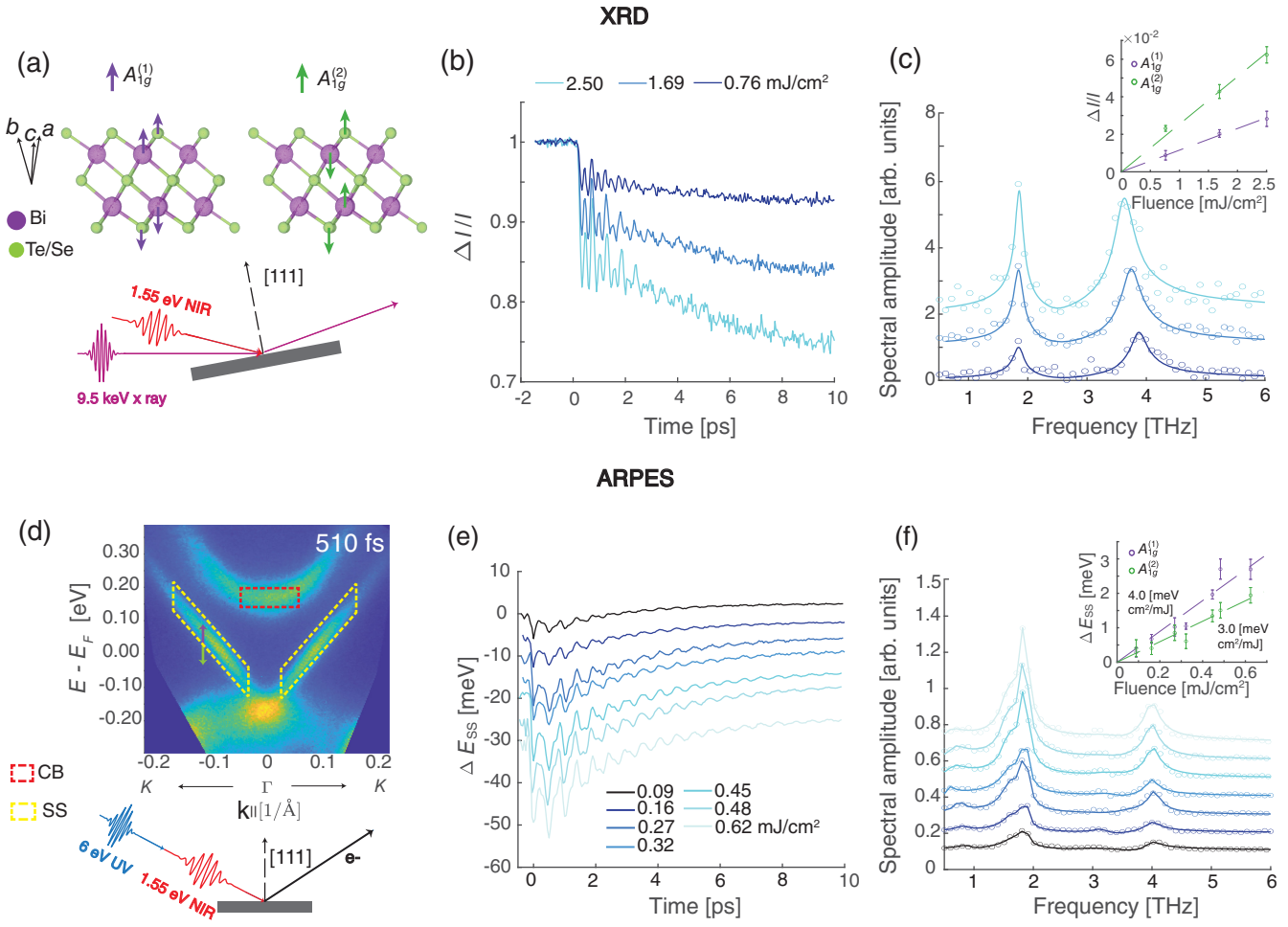

FIG. 1. Room temperature time-resolved measurements on Bi_2Te_3. (a)–(c) Time-resolved XRD. Panel (a) shows two A_{1g} phonon modes of Bi_2X_3 ($X = \mathrm{Se}, \mathrm{Te}$), in purple ($A_{1g}^{(1)}$) and green ($A_{1g}^{(2)}$) arrows, illustrating direction of atomic motion (along [111]) upon photoexcitation of the 1.55 eV laser. In the experiment, x-ray and NIR pulses are both grazing incident to match their penetration depth. Sample normal [111] is demonstrated with broken arrow. (b) Time-resolved diffraction of Bi_2Te_3 (556) peak for different fluences. Data taken at LCLS. (c) Fourier transform of (b). Inset shows linear fluence dependence of $A_{1g}^{(1)}$ and $A_{1g}^{(2)}$ mode induced (556) peak diffraction amplitudes $\Delta I/I$. (d)–(f) Time-resolved ARPES. (d) The electron population at the delay of 510 fs. The boxed area corresponds to a region of interest for the SS (yellow box) and conduction band (CB, red box). In the ARPES experiment, the incident angle of the NIR pump and UV probe are both 50°. The A_{1g} phonon-induced SS shift directions can be obtained from the initial phase of the coherent oscillation, as indicated by purple ($A_{1g}^{(1)}$) and green ($A_{1g}^{(2)}$) arrows. (e) Averaged energy shift of SS (ΔE_{SS}) in the yellow region of interest in (d). (f) Fourier transform of (e). Inset shows linear fluence dependence of SS energy modulation amplitude ΔE_{SS} induced by $A_{1g}^{(1)}$ and $A_{1g}^{(2)}$ mode.

frequency as the modes coupling to the bulk conduction band [51] and we assign them to bulklike $\mathbf{q} = 0$ modes which can be compared to the modes measured by XRD. The amplitudes extracted from LPSVD are linearly dependent on fluence, as shown in Fig. 1(f), inset. We checked the results of LPSVD by comparing the fitted spectra to the real and imaginary parts of the measured Fourier spectrum and found good agreement. Note that as in time-resolved XRD, the phases of each coherent oscillatory component are approximately either 0 or π up to uncertainty of time zero, which suggests that electron band shifts follow adiabatically the ionic motion, consistent with the Born-Oppenheimer approximation and DFT calculations (see below). The electron band shift directions can be annotated as in Fig. 1(d). The fact that both coherent atomic motion and coherent electron band shifts have an initial phase close to 0 or π also allows us to determine the sign of DPs as defined in Eq. (1).

We now discuss the experimental details for measuring the deformation potential of Bi_2Se_3. We performed diffraction measurements at SACLA-FEL on both Bi_2Se_3 and Bi_2Te_3. The pump laser is 1.55 eV, which was

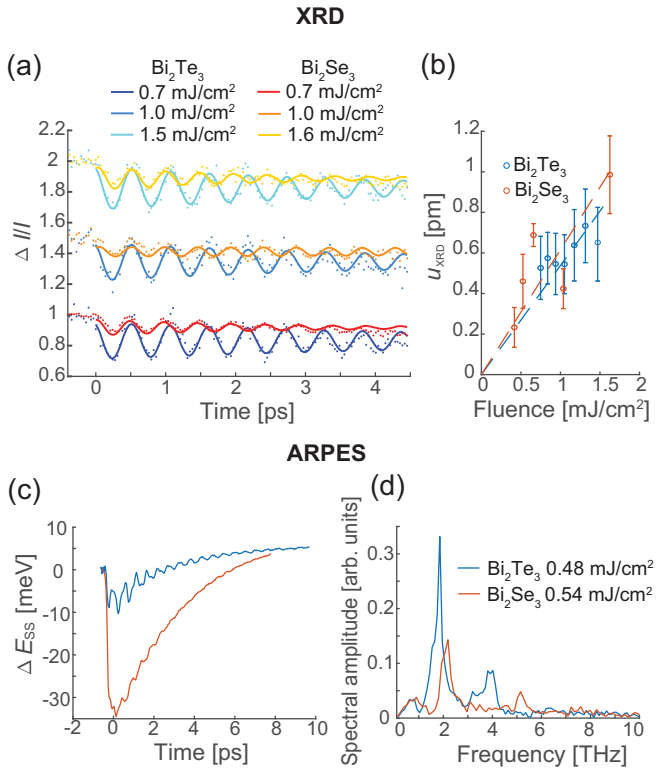

FIG. 2. Room temperature time-resolved measurements comparing photoexcited Bi_2Te_3 and Bi_2Se_3. (a) Bi_2Te_3 and Bi_2Se_3 time-resolved XRD on peak (445) measured at SACLA. The data are grouped into three levels of similar absorbed fluences. The intensity modulation of Bi_2Te_3 is consistently around 3 times larger than Bi_2Se_3. (b) Linear fluence dependence of u^{Bi}. The similar slopes of linear fits on Bi_2Te_3 and Bi_2Se_3 show that their Bi atoms are driven at similar amplitudes. (c) Bi_2Te_3 and Bi_2Se_3 time-resolved ARPES measurements of SS at similar absorbed fluences. (d) Fourier transform of (c).

approximately colinear with the 9.5 keV hard x ray at grazing incidence to the sample. The time resolution is estimated to be 50 fs. In this experiment, Bi_2Se_3 was a 90 nm film on BaF_2 while Bi_2Te_3 was a 200 nm film on sapphire. The two thin film samples were mounted side by side with their surface normals aligned to within the order of 0.01°. This alignment ensures that systematic errors in the incident fluence calibration between the two materials are negligible in the XRD experiment.

Figure 2(a) shows raw data (dots) and fit (solid lines) of the Bi_2Te_3 and Bi_2Se_3 diffraction intensities on Bragg peak (445). Data are grouped by similar absorbed fluence after accounting for differences in the film thickness and optical absorption (see Appendix D) and offset for clarity. Since the $A_{1g}^{(2)}$ mode was not resolved in Bi_2Se_3, we only present the atomic motion of the $A_{1g}^{(1)}$ mode. From Fig. 2(a), the diffraction intensity modulations of the Bi_2Te_3 $A_{1g}^{(1)}$ mode are consistently about 3 times larger than in Bi_2Se_3. Meanwhile, the (445) peak sensitivity to $A_{1g}^{(1)}$ distortion is about 3 times larger in Bi_2Te_3 than in Bi_2Se_3, due to their different eigenvectors. Therefore, the computed displacements u_{XRD} of $A_{1g}^{(1)}$ in the two materials are concluded to be similarly driven, see Fig. 2(b), where the slope of linear fit (broken lines) to Bi_2Te_3 is a factor of 0.88 lower than Bi_2Se_3.

The SS energy shifts in Bi_2Se_3 were measured with time-resolved ARPES under the same conditions as Bi_2Te_3, but with a slightly worse time resolution of 85 fs. In Fig. 2(c) we show the SS energy shifts for both materials at similar absorbed fluences. As seen from the Fourier transforms in Fig. 2(d), Bi_2Se_3 has both $A_{1g}^{(1)}$ (2.2 THz) and $A_{1g}^{(2)}$ (5.2 THz) phonons, similar to Bi_2Te_3. The frequencies of Bi_2Se_3 A_{1g} phonons are higher than those in Bi_2Te_3 largely due to the lower average atomic mass. Analysis of the ARPES data shows that while the overall band shift is substantially larger in Bi_2Se_3, the oscillatory component corresponding to the $A_{1g}^{(1)}$ mode in Bi_2Te_3 is a factor of 2.05 larger than in Bi_2Se_3 for the same fluence.

Though we only focus on the coherent components of the time-resolved ARPES signal, we offer several possible reasons for the exponentially decaying incoherent background. A possible contribution to band-shifting dynamics is from surface photovoltage, which generates long-range electric fields that couple to the photoelectron trajectories following photoexcitation. The other contribution may be from electronic heating effects and the ensuing coupling of electrons to other excitations, including other electron-phonon coupling channels. As the electrons cool they generate phonons throughout the Brillouin zone in an incoherent fashion. These effects can be material dependent. But we emphasize that we only extract the magnitude of the shift from the coherent oscillation amplitude (up to correction factors discussed from here on).

III. CALCULATION OF DEFORMATION POTENTIALS

This section first discusses the calculations of Bi_2Te_3 DPs, which use numerical simulation to correct for intrinsic and extrinsic effects. We separately consider each effect below to provide the reader with intuition about the various ingredients and how to estimate their relative contributions. We then discuss the calculations of Bi_2Se_3 DP, which is based on properly scaling the results of Bi_2Te_3 we established previously.

A. Calculations for Bi_2Te_3: Intrinsic effects

To compute the DP from experimental quantities, ideally, the measurements would be performed under identical pump conditions. For a given sample and pump wavelength, it means measurements would be performed at the

same fluence F. Experimentally, it is convenient to measure the linear F dependence of the displacements and energy shifts, and use the fitted slopes to determine the DP:

$$\mathrm{DP} = \frac{(d\Delta E_{\mathrm{SS}}/dF)}{(du_{\mathrm{SS}}/dF)}. \tag{2}$$

ARPES measures directly the SS energy shift (ΔE_{SS}), while XRD measures a weighted average of the atomic displacements over the probed region of the sample ($u_{\mathrm{XRD}} \neq u_{\mathrm{SS}}$). Above we defined u_{SS} in Eq. (1) as a weighted average over the SS wave function extension. This brings uncertainties intrinsically related to the nature of the measurements which need to be addressed before Eq. (2) can be applied to compute the DP. To address this, we rescale the XRD measurements to give the atomic displacements in the vicinity of the SS:

$$u_{\mathrm{SS}} = \left(\frac{\tilde{u}_{\mathrm{SS}}}{\tilde{u}_{\mathrm{XRD}}}\right) u_{\mathrm{XRD}}. \tag{3}$$

Quantities with tildes are obtained from simulations. The factor $(\tilde{u}_{\mathrm{SS}}/\tilde{u}_{\mathrm{XRD}})$ is the simulated ratio between the average displacement $\tilde{u}_{\mathrm{SS}}$ over the spatial extent of the SS and the average displacement $\tilde{u}_{\mathrm{XRD}}$ measured by XRD. As we shall show, this ratio can be calculated by modeling the generation process of the depth-dependent coherent phonon field $u(z,t)$. For conceptual clarity, we begin by neglecting diffusion and recombination, and return to examine them later in this section.

The depth dependence of XRD is given by the x-ray penetration depth, which, for Bi_2Te_3, is 55 nm for our experimental condition (x-ray grazing incident at 0.5°. In contrast, the SS wave function extends only ~1 nm from the surface [52]. These length scales are denoted by $1/\alpha_i$, where ($i = \mathrm{XRD}$) corresponds to the x-ray penetration depth at the incident angle in an XRD measurement, and ($i = \mathrm{SS}$) corresponds to the spatial extent of the SS wave function. The change in scattering intensity in XRD is taken to be a weighted average of the phonon amplitude over the probed region. Similarly, the energy oscillation of the SS is given by displacements averaged over the extent of its wave function. These weighted averages can be written:

$$\tilde{u}_i(t) = \frac{\int_0^{L_i} dz \exp(-\alpha_i z) u(z,t)}{\int_0^{L_i} dz \exp(-\alpha_i z)}, \tag{4}$$

where L_i represents the thickness of the sample. To compute the displacements $u(z,t)$, we model $u(z,t)$ as a harmonic oscillator displaced to a new quasiequilibrium coordinate $u'(z,t)$ [45]:

$$\frac{d^2u}{dt^2} = -(2\pi f)^2[u(z,t) - u'(z,t)] - \gamma \dot{u}(z,t), \tag{5}$$

where f is the frequency and γ is the damping rate. The displaced coordinate $u'(z,t)$ is proportional to the photoinduced carrier density $n(z,t)$, which has the initial condition:

$$n(z, t=0) \propto \exp(-\alpha_0 z), \tag{6}$$

where α_0 ($1/\alpha_0 = 15$ nm) is the absorption coefficient of the pump. Neglecting diffusion and recombination, the carrier density is static, and Eq. (6) is applicable for all times $t > 0$; that is, $n(z, t>0) = n(z, t=0)$. From Eqs. (4) and (6) we obtain

$$\tilde{u}_i = u_0 \frac{\alpha_i}{\alpha_i + \alpha_0} \frac{1 - e^{-(\alpha_0+\alpha_i)L_i}}{1 - e^{-\alpha_i L_i}}, \tag{7}$$

where u_0 represents the displacement at $z = 0$. We find that the rescaling factor is $(\tilde{u}_{\mathrm{SS}}/\tilde{u}_{\mathrm{XRD}}) = 2.6$, which shows that XRD probes a deeper region in which the weighted average displacements are substantially attenuated compared to the surface.

We now examine the possible role of carrier diffusion and recombination, which redistribute carriers following photoexcitation and can therefore introduce a time and depth dependence to the phonon driving forces. To motivate this discussion, we compute a back-of-the-envelope estimate of the relevance of diffusion: Using the carrier diffusivity of Bi_2Te_3, $D_e = 520$ nm^2/ps [53], we estimate a characteristic diffusion timescale of $1/(D_e\alpha_0^2) \approx 0.4$ ps. This is comparable with the phonon period for $A_{1g}^{(2)}$ of 0.25 ps. We conclude that diffusion redistributes carriers on a timescale comparable to that of the coherent phonon generation process, and its effect on the driving forces should be investigated.

To quantitatively model the effect, we retain Eq. (6) as an initial condition but allow the distribution to evolve via diffusion along the sample normal direction $\hat{z}$:

$$\frac{dn}{dt} = D_e \frac{d^2n}{dz^2} - \frac{1}{\tau_0} n, \tag{8}$$

where τ_0 is the carrier lifetime, which is estimated to be 20 ps [54]. We apply a boundary condition,

$$\frac{dn}{dz}(z=0) = 0, \qquad \frac{dn}{dz}(z=L_i) = 0, \tag{9}$$

to enforce no diffusion across the sample boundaries at 0 and L_i.

We obtain the carrier density profile $n(z,t)$, by solving Eq. (8). To connect this to our experiment, we can then compute the coherent phonon amplitude $u(z,t)$ from Eq. (5) by taking $u'(z,t) \propto n(z,t)$ as before, but now with the time dependence included. However, for the most faithful modeling of the experiment, we must account

for the fact that the phonon frequency is itself a function of $n(z,t)$, as demonstrated experimentally by fluence-dependent mode softening in Fig. 9(a). We model this as a linear dependence of the mode frequency $f(z,t)$ on fluence: $f(z,t) = f_0[1 - \beta n(z,t)]$. Here f_0 is the equilibrium frequency and $\beta > 0$ is the proportionality constant which determines the magnitude of the softening. With this assumption, we can numerically solve for $u(z,t)$, and finally calculate the average displacements $\tilde{u}_i(t)$ using Eq. (4).

Here we take the $A_{1g}^{(2)}$ mode as an example, and describe the simulation of Bi_2Te_3, assuming $D_e = 520\ \mathrm{nm}^2/\mathrm{ps}$ [53]. We choose β to reproduce the observed linear softening, as shown in Appendix C. The damping constant γ is taken to be $0.25\ \mathrm{ps}^{-1}$, to be consistent with the experimental data. We find that $(\tilde{u}_{\mathrm{SS}}/\tilde{u}_{\mathrm{XRD}}) = 2.2$ for $A_{1g}^{(2)}$. The corresponding factor for the $A_{1g}^{(1)}$ mode is 2.0. These can be compared with the factor of 2.6 we computed earlier from Eq. (7), which neglected diffusion and recombination. This indicates that the carrier dynamics introduce a 20%–30% correction on top of the penetration depth considerations. Therefore, for quantitative purposes it is necessary to account for diffusion and recombination; however, the dominant correction arises from the large penetration depth of the XRD measurement compared to the extent of the SS wave function.

B. Calculations for Bi_2Te_3: Extrinsic effects

We now return to the issue of extrinsic effects. The first is the experimental uncertainty of fluence measurements in different experimental facilities. The second is the correction required by different time resolutions τ in ARPES and XRD measurements.

The precision and accuracy of fluence measurements can vary substantially between different labs: in published Bi measurements, the reported fluences for the same amount of phonon softening differ by up to a factor of 5 in independent measurements [55–58]. These discrepancies may be attributed to miscalibration in the laser power measurement or errors in the measurement of the incident area on the sample. Therefore, for quantitative calculation of the DP, we investigate fluence uncertainties between XRD and ARPES measurements.

Fluence uncertainties can be calibrated by using the $A_{1g}^{(2)}$ frequency as a proxy due to its strong dependence on fluence, as shown in Appendix C. Explicitly, we need to define

$$u_{\mathrm{SS}} = \frac{(d\tilde{u}_{\mathrm{SS}}/d\tilde{f}_{\mathrm{SS}})}{(d\tilde{u}_{\mathrm{XRD}}/d\tilde{f}_{\mathrm{XRD}})} u_{\mathrm{XRD}} \tag{10}$$

in place of Eq. (3), and accordingly

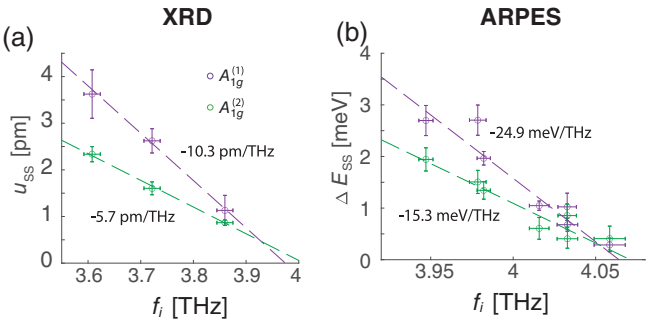

FIG. 3. $A_{1g}^{(2)}$ frequency dependence in Bi_2Te_3. (a) Displacement u_{SS} and (b) SS band shift ΔE_{SS} as a function of the measured $A_{1g}^{(2)}$ frequency.

$$\mathrm{DP} = \frac{(d\Delta E_{\mathrm{SS}}/df_{\mathrm{SS}})}{(du_{\mathrm{SS}}/df_{\mathrm{XRD}})}, \tag{11}$$

where f_i is the $A_{1g}^{(2)}$ frequency measured by the respective techniques. We note that $f_{\mathrm{SS}} \neq f_{\mathrm{XRD}}$ even for the same incident fluence F. This is again due to the depth dependence of phonon fields, and the different sensitivities of ARPES and XRD as described by Eq. (4). Equation (11) is mathematically equivalent to the original definition [Eq. (2)]. By doing so, uncertainties in fluence calibration are effectively circumvented by using the softened frequency as a proxy. The calculation of $(d\tilde{u}_{\mathrm{SS}}/d\tilde{f}_{\mathrm{SS}})/(d\tilde{u}_{\mathrm{XRD}}/d\tilde{f}_{\mathrm{XRD}})$ is detailed in Appendix C.

Both measured quantities u_{XRD} and ΔE_{SS} need to be multiplied by an additional correction factor due to limited time resolution τ (60 fs in ARPES and 50 fs in XRD measurements) [44,59]:

$$\exp\left(-\frac{\pi^2 f_0^2 \tau^2}{4\ln 2}\right), \tag{12}$$

where f_0 represents A_{1g} mode frequency f_0.

Equation (11) is then used to calculate DPs of A_{1g} modes in Bi_2Te_3. In Fig. 3(a), we plot the displacement u_{SS} and the electronic band shift ΔE_{SS} as a function of $A_{1g}^{(2)}$ frequency. The slopes of these linear fits are used to calculate the DPs in Eq. (11). The resulting DPs are listed in Table I, which reflects our best estimate considering all intrinsic and extrinsic factors. We note that these values differ by 20% compared with the DP calculation results without using frequency as a proxy for fluence, suggesting a fluence mismatch of 20% between the two measurement facilities.

The error bars in the table are estimated as follows. Statistical errors are obtained from the fitting error bars of Figs. 3(a) and 3(b) which weighs in both the horizontal error bars and vertical error bars. Systematic errors are estimated based on the uncertainty in two important parameters of our calculation: the x-ray incidence angle

TABLE I. Deformation potential (meV/pm). The experimental values are averaged over the region of interest across $\mathbf{k}_{||}$ space as shown in Fig. 1(d). The experiment values account for intrinsic and extrinsic corrections. Error bars include both systematic and statistical error. Theory values are taken at the Γ point. The signs of the DFT DPs [defined according to the displacements and shifts shown in Figs. 1(a) and 1(d)] are the same as measured by the experiment.

	Experiment	Theory (LDA)
Bi_2Te_3, $A_{1g}^{(1)}$	2.4 (0.7)	5.8
Bi_2Te_3, $A_{1g}^{(2)}$	2.7 (0.8)	6.8
Bi_2Se_3, $A_{1g}^{(1)}$	1.8 (0.7)	1.2

(and hence the penetration depth) and the magnitude of the diffusivity. We estimate a ±0.1° uncertainty with respect to the nominal incidence angle 0.5°, which results in penetration depths ranging from 35 to 70 nm. This introduces an error of 8% into DP calculation. To estimate the systematic error associated with diffusivity, we varied the value from 200 to 1000 nm^2/ps, which differs from the estimated value of $D_e = 520\ nm^2/ps$ by roughly a factor of 2. This introduces a corresponding 15% uncertainty in the DP. We note that the above assumes only majority carrier diffusivity, but the ambipolar diffusivity falls well within the range of uncertainty [60]. Although there can be a change in the diffusivity upon photoexcitation [61,62], we expect it to quickly return to its near equilibrium level as the photoexcited carriers relax.

C. Calculation for Bi_2Se_3

To compute the DP of Bi_2Se_3, we cannot directly employ the strategies from the previous section (Sec. II B) that minimize the systematic errors due to fluence calibration. The $A_{1g}^{(2)}$ mode of Bi_2Se_3 was not observed by XRD, and is therefore not available as a fluence proxy. Instead, we exploit that Bi_2Se_3 and Bi_2Te_3 were measured side by side by XRD and thus without systematic fluence uncertainty. This allows us to compute the ratio of their DPs as defined in Eqs. (3) and (2):

$$\mathrm{DP} = \left(\frac{\tilde{u}_{\mathrm{SS}}}{\tilde{u}_{\mathrm{XRD}}}\right)^{-1} \frac{(d\Delta E_{\mathrm{SS}}/dF)}{(du_{\mathrm{XRD}}/dF)}. \tag{13}$$

From the XRD measurements at SACLA and the ARPES measurements as shown in Fig. 2, we obtain the ratio 2.33 of the quantity $(d\Delta E_{\mathrm{SS}}/dF)/(du_{\mathrm{XRD}}/dF)$ between Bi_2Te_3 and Bi_2Se_3.

We then need to take into account that the carrier diffusivity in Bi_2Se_3 is much higher, $D_e = 1400\ nm^2/ps$ [63]. Diffusion, therefore, leads to a lower carrier density in the vicinity of the SS in Bi_2Se_3 as compared to Bi_2Te_3, leading to a lower $\tilde{u}_{\mathrm{SS}}$, and thus an additional correction factor of 0.63 to the ratio of DPs between Bi_2Te_3 and Bi_2Se_3, due to the quantity $(\tilde{u}_{\mathrm{SS}}/\tilde{u}_{\mathrm{XRD}})$. See Appendix C for more details. Lastly, we account for the correction due to time resolution differences, which introduces a factor of 0.93. We arrive at the final DP ratio of Bi_2Te_3 over Bi_2Se_3 of 1.37.

Finally, knowing the $A_{1g}^{(1)}$ DP ratio we can calculate the absolute value Bi_2Se_3 DP based on our knowledge of the Bi_2Te_3 DP value; see Table I. The uncertainties include statistical error (32%), as well as systematic error (16%) from uncertainties in x-ray incidence angle calibration and carrier diffusivities.

The nonobservation of Bi_2Se_3 $A_{1g}^{(2)}$ mode in the SACLA XRD measurement is attributed to the limited time resolution and the considerable x-ray beam intensity fluctuations. Based on the peak sensitivity and the noise level, we estimate an upper bound of the $A_{1g}^{(2)}$ mode atomic displacement in Bi_2Se_3, and thus lower bound of the Bi_2Se_3 $A_{1g}^{(2)}$ DP of 0.2 meV/pm.

IV. DFT CALCULATIONS

We performed DFT calculations to compare with the experimentally measured A_{1g} SS DPs of Bi_2Te_3 and Bi_2Se_3. The details of our calculations are given in Appendix E. The computed electronic band structures of Bi_2Te_3 and Bi_2Se_3 slabs are shown in Figs. 4(a) and 4(b). DPs are obtained using the frozen phonon method, where the atoms are displaced along the A_{1g} mode coordinates [as defined in Fig. 1(a)], and the SS energy shifts are calculated based on the resulting shifts in the electronic band structure of a slab [as defined in Fig. 1(d)]. In our DP calculations, we use the vacuum level of the Hartree potential to align the energies of the electronic states. We assume that bulk phonon modes are homogeneously distributed along the slab despite the surface's presence. The computed DPs along K-Γ-M are shown in Figs. 4(c) and 4(d). They do not exhibit considerable anisotropy in the range of $\mathbf{k}$ values presented in Figs. 4(c) and 4(d). However, the calculated DPs become more anisotropic in the wider $\mathbf{k}$ range due to strong warping effects along the Γ-M direction [64,65].

We select the computed DP values at the Γ point to compare with the experimental values, and include them in Table I. The calculated $A_{1g}^{(1)}$ DP in Bi_2Se_3 is 1.5 times smaller than in the experiment. We consider that they agree within the experimental uncertainties. In Bi_2Te_3, the A_{1g} DPs are about 2.5 times larger than the experimental values and outside of the estimated confidence interval of measurements. We emphasize that this comparison does not reveal an order of magnitude difference as found in the strongly correlated superconductor FeSe [44] and that our values are roughly one order of magnitude smaller than those for other nontopological semiconductors such as Si and Ge [66]. Considering the theoretical and experimental

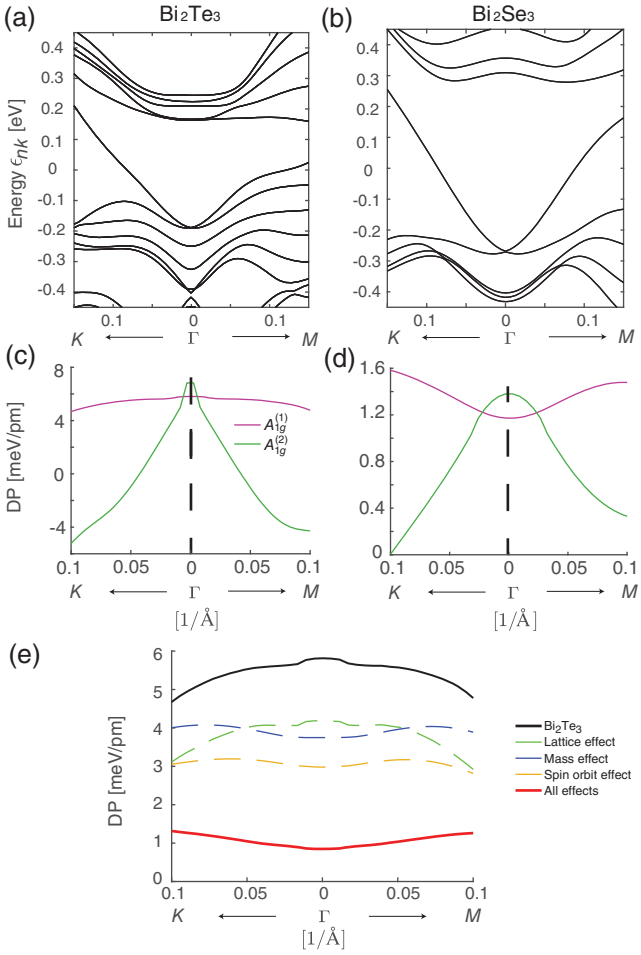

FIG. 4. DFT calculation of electronic band structures and deformation potentials. (a) Band structure for a 6-quintuple layer (QL) slab of Bi_2Te_3, shown for part of the reciprocal space. (b) Band structure for a 5-QL slab of Bi_2Se_3. (c) Deformation potential (DP) of the two A_{1g} modes in Bi_2Te_3 derived from frozen phonon calculations. (d) Deformation potentials of the A_{1g} modes in Bi_2Se_3. (e) Calculated A_{1g} mode DP by swapping the lattice constants value, masses of group-VI atoms, and spin-orbit coupling strength in Bi_2Te_3 with that of Bi_2Se_3. Combining all three effects, the prediction of factor 4.8 larger A_{1g} DP in Bi_2Te_3 can be reasonably explained.

difficulties in obtaining precise and accurate values on a scale of a few meV per unit cell, we regard a difference of factor 2 as general agreement. We also note the consistent signs of experimentally derived and theoretically obtained DPs.

From the perspective of theory, it is interesting that calculations for the $A_{1g}^{(1)}$ mode predict a factor 4.8 larger DP in Bi_2Te_3 than in Bi_2Se_3. This only agrees qualitatively with the experiment which observed a factor 1.4 larger DP in Bi_2Te_3. This quantitative discrepancy might be attributed to the limitations of DFT calculations in capturing the precise band structure. We note that in the experiment, the $A_{1g}^{(1)}$ DPs are weakly momentum dependent near the zone center (see Appendix B), whereas theory predicts strong momentum dependence of the $A_{1g}^{(2)}$ DPs. Calculations that account for electron correlations may result in a better agreement with the experimentally measured band structure, as suggested by Ref. [67], as well as our DP measurements.

To understand the difference in the DP values of Bi_2Te_3 and Bi_2Se_3 computed with DFT, we conducted a numerical experiment in which we modified individual parameters that are different in the two systems. These are lattice constants, Se and Te atomic masses, and the spin-orbit coupling strength. This thought experiment sheds light on the individual contributions of these parameters to the DPs in both materials.

We start with Bi_2Te_3 and evaluate the contribution of each individual parameter of Bi_2Se_3 to the DPs of Bi_2Te_3. Note that we varied only one parameter at a time, while holding the rest at their nominal values for Bi_2Te_3. The resulting $A_{1g}^{(1)}$ deformation potentials are plotted in Fig. 4(e). If the Se atomic mass replaces the Te atomic mass, the DP is reduced by ∼35% due to the change in eigenvector (see Table II). By modifying the spin-orbit interaction strength of Te to the value in Se, the DP is reduced by ∼50%. When the Bi_2Se_3 lattice parameters are used for the Bi_2Te_3 system, the DP at Γ is reduced by ∼27%, which is mostly related to the lattice expansion affecting the crystal field splitting. Finally, when all these factors are simultaneously incorporated, Bi_2Te_3 is effectively transformed into Bi_2Se_3, reproducing the factor ∼5 difference of native local-density approximation (LDA). Our numerical experiment demonstrates that no single factor is sufficient to explain the difference in the calculated DPs of Bi_2Te_3 and Bi_2Se_3, and that lattice constants, atomic masses, and spin-orbit coupling strength are all key ingredients.

Additionally, we performed a constrained DFT calculation (see Appendix E) of the vibrational modes for the photoexcited bulk Bi_2Te_3 and Bi_2Se_3. We found that for Bi_2Te_3, the mode amplitude dependence on $A_{1g}^{(1)}$ frequency reproduces the measurement well, and that the ratio between Bi_2Te_3 and Bi_2Se_3 phonon amplitudes for the same excitation density, as well as the atomic motion directions, are consistent with the experiment.

V. CONCLUSIONS

We combined time-resolved XRD and ARPES measurements on the topological insulators Bi_2Te_3 and Bi_2Se_3 and quantified the coupling between topological surface states and A_{1g} phonon modes by extracting mode- and band-resolved deformation potentials. We compare experimental results to DFT and find reasonable agreement. Our results directly impact the microscopic understanding of topological SS transport and topological

phase transitions [28]. Our methodology lays the systematic groundwork required for future work studying electron-phonon coupling in more complex quantum materials.

For the dominant $A_{1g}^{(1)}$ phonon mode, we find a DP on the order of 2 meV/pm in both materials. The coupling is 1.4 times larger in Bi_2Te_3 than in Bi_2Se_3, yet this difference is insignificant within experimental uncertainties. Our DFT calculations agree with the experimental findings within a factor of 2.5, which we regard as agreement considering the small energy and length scales involved. While we cannot exclude that correlation effects in the calculations might improve agreement with the experiment, we did not observe an order of magnitude discrepancy as was revealed for the strongly correlated superconductor FeSe [44]. In addition, excited state DFT correctly predicts the experimentally observed mode softening. We also analyzed the individual contributions of lattice constants, atomic masses, and spin-orbit coupling strength to the difference between the DFT values of DPs for Bi_2Te_3 and Bi_2Se_3. All parameters contribute considerably, with spin-orbit coupling providing the largest contribution. These favorable results underline that DFT in this material class is well capable of predicting how photoexcited electrons couple to phonon modes and of capturing excited potential energy surfaces.

We performed a comprehensive analysis of correction factors due to intrinsic and extrinsic experimental effects. The most substantial intrinsic effect is the different depth sensitivity of the two probes, which leads to a different mismatch of pumped and probed sample volumes. Only smaller corrections are necessary to account for photoexcited carrier diffusion and recombination. Extrinsic effects are dominated by uncertainties of the excitation density. We were able to circumvent this extrinsic issue by using a strongly fluence-dependent phonon mode frequency as inherent calibration.

Our insights hold important positive lessons for future work. The strongest intrinsic effect of different probing depths can be greatly reduced by experiments on films thinner than the pump's optical penetration depth. This ensures a homogeneous distribution of excited carriers regardless of the probe penetration depth and also mitigates diffusion effects. This approach taken in Ref. [44] results in only a modest factor of 1.03 to account for the different penetration depths of ARPES and XRD.

Looking further ahead, we suggest using higher and tunable photon energies for time-resolved ARPES. This will allow accessing the dynamics of bulk states in well-defined conditions, which this work was not able to accomplish. We expect that future multimodal experiments will combine time-resolved ARPES and diffraction methods in a single instrument. Most if not all extrinsic effects will be eliminated in such simultaneous experiments. Free-electron laser facilities will provide this platform to open a new experimental paradigm for studying electron-phonon coupling with high accuracy and precision.

ACKNOWLEDGMENTS

Y. H., J. A. S., S. W. T., M. T., P. S. K., T. H., M. J., Z-X. S., and D. A. R. were supported by the U.S. Department of Energy, Office of Science, Office of Basic Energy Sciences through the Division of Materials Sciences and Engineering under Contract No. DE-AC02-76SF00515. Use of the LCLS and S. S. R. L. is supported by the U.S. Department of Energy, Office of Science, Office of Basic Energy Sciences under Contract No. DE-AC02-76SF00515. The SACLA experiment was performed with the approval of the Japan Synchrotron Radiation Research Institute (JASRI; Proposal No. 2018B8079). T. K. acknowledges JSPS KAKENHI (Grants No. JP19H05782, No. JP21H04974, and No. JP21K18944). The DFT work was supported by Science Foundation Ireland and the Department for the Economy Northern Ireland Investigators Program under Grants No. 15/IA/3160 and No. 12/IA/1601. Preliminary x-ray characterization was performed at beam line 7-2 at the Stanford Synchrotron Radiation Lightsource (SSRL). The ellipsometry measurement and thin film reflection measurement were performed at the Stanford Nano Shared Facilities (SNSF), supported by the National Science Foundation under Grant No. ECCS-2026822. Y. H. acknowledges help with SACLA beam time from Christopher P. Weber, Matthew J. Kim, and Ka Lun Michael Man. Y. H. and D. A. R. also thank Christopher P. Weber for suggestions on the manuscript.

APPENDIX A: CRYSTAL STRUCTURES

Figure 5 shows the crystal structure of space group $R\bar{3}m$, and provides a 1D-atom-chain view of $A_{1g}^{(1)}$ mode on the right-hand side. The quintuple-layer view of $A_{1g}^{(1)}$ mode as Fig. 1(a) is provided in the pink box. The layer pattern is represented with A, B, and C. Atoms forming the 1D atom chain are all taken from the A layer. The primitive unit cell is outlined with gray solid lines. Among the three types of atoms participating in A_{1g} modes, Bi, $X(\mathrm{I})$, and $X(\mathrm{II})$, the $X(\mathrm{I})$ atoms are not allowed to displace in a A_{1g} mode as these atoms are the centers of inversion symmetry. Thus, an A_{1g} phonon has only 2 degrees of freedom determined by Bi and $X(\mathrm{II})$ atomic motion along [111]. Since there are two free parameters, there are correspondingly two A_{1g} modes.

First, we refine the internal atomic coordinates using the static diffraction intensity on different peaks. Second, to determine the eigenvector, we use the diffraction intensity modulation induced by the same phonon mode measured across multiple Bragg peaks. Finally, based on the

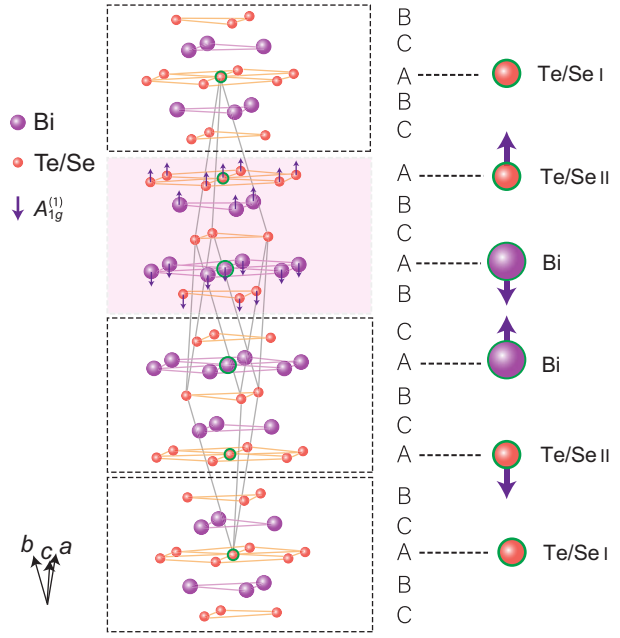

FIG. 5. Crystal structure of Bi_2X_3 ($X = Se, Te$) and schematic for $A_{1g}^{(1)}$ phonon mode.

measured eigenvectors, u_λ^{Bi} can be quantified from diffraction. We detail the second step below.

We parametrize the $X(II)$ atom coordinates in the primitive unit cell as $(\delta_1, \delta_1, \delta_1)$ and the Bi atom coordinates as $(\delta_2, \delta_2, \delta_2)$. Then the scattering structure factor is given by

$$F = f_X + 2e^{i\pi(h+k+l)}\{f_X \cos[\pi(1-2\delta_1)(h+k+l)] + f_{Bi}\cos[\pi(1-2\delta_2)(h+k+l)]\}, \quad \text{(A1)}$$

with $\delta_1 \approx \frac{1}{5}$ and $\delta_2 \approx \frac{2}{5}$. For Bragg peaks, h, k, l are integers, and we define $h+k+l = N$. For $N = 5n$, the Bragg peaks are not sensitive to either of the A_{1g} modes. For $N = 5n \pm 1$, peaks have the same sensitivity to a given A_{1g} mode for a given n, and are sensitive to both $A_{1g}^{(1)}$ and $A_{1g}^{(2)}$. For $N = 5n \pm 2$, peaks have the same sensitivity to a given A_{1g} mode for a given n, and are sensitive mainly to the $A_{1g}^{(1)}$ mode.

During the XRD experiment at LCLS we oriented the sample by rotating it around the azimuthal axis, which was aligned to the sample surface normal to within 0.1°. We so obtained the static x-ray scattering intensity on a total of seven peaks. This allows us to refine the lattice constants and the internal coordinates (δ_1, δ_2), which are in good agreement with DFT calculations.

The eigenvector of Bi_2Te_3 A_{1g} phonon mode can be obtained from the intensity modulation amplitude of a set of peaks sensitive to the mode. We need only one free parameter to describe two A_{1g} mode eigenvectors simultaneously, and we pick this free parameter to be the Bi/Te ratio in the $A_{1g}^{(1)}$ mode. The experimental observables are the Bragg peak intensity modulations induced by an A_{1g} mode [Figs. 6(a) and 6(b)]. As shown in Figs. 6(c) and 6(d), amplitudes of the normalized Bragg peak intensity modulation $\Delta I/I$ linearly increase with fluence. The increase in $\Delta I/I$ per unit fluence (1 mJ/cm^2) is the slope of the linear fit constrained through the origin in Figs. 6(c) and 6(d).

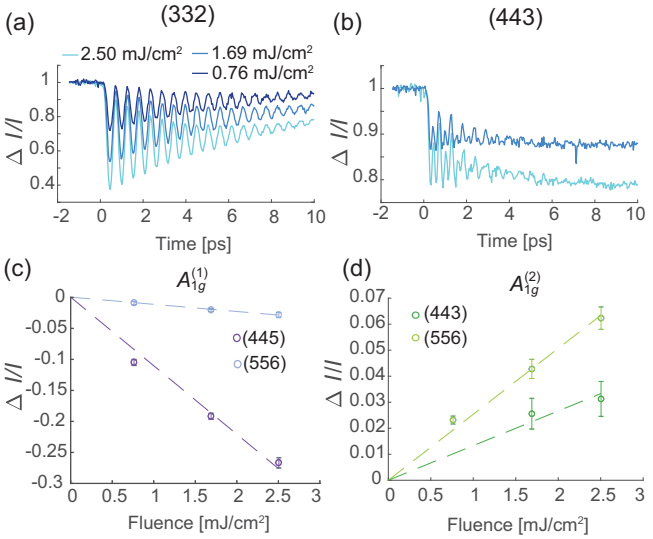

FIG. 6. Bi_2Te_3 XRD data from LCLS for the eigenvector reconstruction. (a),(b) Time-resolved diffraction on peaks (332) and (443). Peak intensity modulation amplitude induced by a given A_{1g} mode is different on peaks (332) and (443), which contains information for calculating the A_{1g} eigenvector. (c) $A_{1g}^{(1)}$ induced normalized intensity modulation amplitude $\Delta I/I$ on peaks (445) and (556). (d) $A_{1g}^{(2)}$ induced intensity modulation amplitude on peaks (443) and (556).

We aim to solve for three unknown variables: (1) the Bi/Te ratio in the $A_{1g}^{(1)}$ mode, (2) the $A_{1g}^{(1)}$ mode amplitude (alternatively one can also choose to use u^{Bi}) increase per unit fluence, and (3) the $A_{1g}^{(2)}$ mode amplitude increase per unit fluence. We therefore define a set of three constraining equations: the linear slopes of (1) the $A_{1g}^{(1)}$ modulated diffraction intensity of the (556) peak versus fluence, (2) the $A_{1g}^{(1)}$ modulated diffraction intensity of the (445) peak versus fluence, and (3) the $A_{1g}^{(2)}$ modulated diffraction intensity of the (556) peak versus fluence. To avoid near degeneracy of the equation set, we pick two peaks that satisfy either $N = 5n \pm 1$ or $N = 5n \pm 2$ for the $A_{1g}^{(1)}$ mode. The solution of this equation set agrees with the eigenvectors calculated by DFT to within 15%, when comparing the *normalized* $A_{1g}^{(1)}$ eigenvector projected onto a Bi atom.

TABLE II. The normalized eigenvectors of Bi_2Te_3 and Bi_2Se_3 A_{1g} modes. Bi_2Te_3 eigenvectors are obtained using XRD, while those of Bi_2Se_3 are calculated using DFT.

Mode	Bi	Te/Se II
Bi_2Te_3, $A_{1g}^{(1)}$	0.44	−0.56
Bi_2Te_3, $A_{1g}^{(2)}$	0.56	0.44
Bi_2Se_3, $A_{1g}^{(1)}$	0.58	−0.40
Bi_2Se_3, $A_{1g}^{(2)}$	0.40	0.58

Table II shows the normalized eigenvectors of Bi_2Te_3 calculated through XRD measurements, and of Bi_2Se_3 obtained through DFT. For Bi_2Se_3 we did not resolve signals on a sufficient number of Bragg peaks to directly solve the eigenvectors.

APPENDIX B: k DEPENDENCE OF SS ENERGY SHIFTS

To enhance the signal-to-noise ratio of the surface electron band coherent oscillations, we average the change in band energy over ± 0.2 Å^{-1} near Γ, which is based on the fact that the DPs and thus the electron band shifts are nearly constant across this area of reciprocal space. In Fig. 7 we show the **k**-dependent SS response: the sampled $\mathbf{k}_{||}$ points are illustrated in Figs. 7(a) and 7(d). In Figs. 7(g) and 7(h), the energy shift versus A_{1g} frequencies for different $\mathbf{k}_{||}$ points are plotted for $A_{1g}^{(1)}$ and $A_{1g}^{(2)}$ in Bi_2Te_3. The $\mathbf{k}_{||}$ dependence of $A_{1g}^{(1)}$-induced binding energy oscillations $\Delta E^{n\mathbf{k}}$ is weak with a variation of 13%. The $A_{1g}^{(2)}$ has a lower signal-to-noise ratio, adversely impacting the amplitude

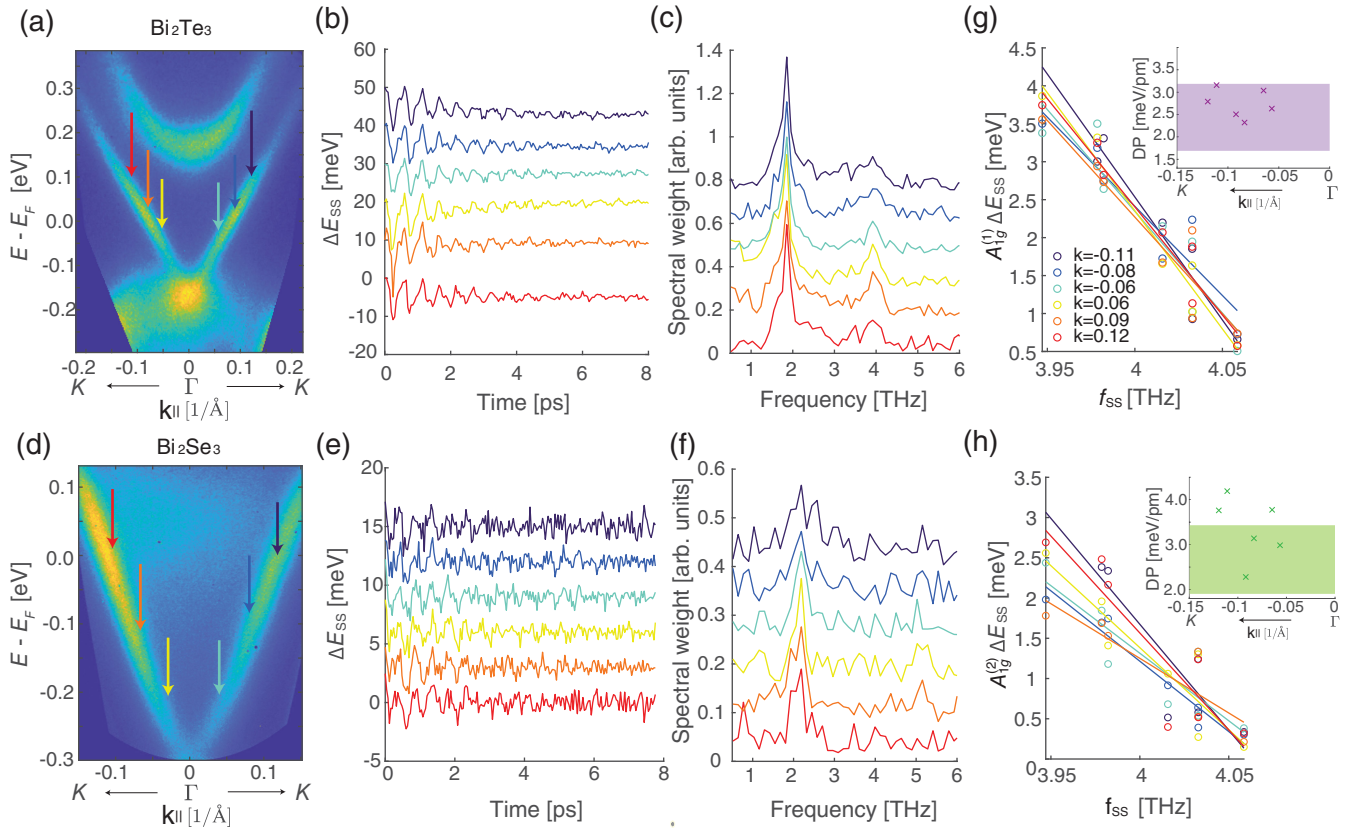

FIG. 7. **k** dependence of time-resolved ARPES measurements. (a) The electron population of Bi_2Te_3 measured at 510 fs delay at 1.02 mJ/cm^2. The arrows show different $\mathbf{k}_{||}$ regions we sample for the SS. (b) Modulation of Bi_2Te_3 SS at 1.02 mJ/cm^2, sampled at different $\mathbf{k}_{||}$ regions. An incoherent background in the form of an exponential decay has been subtracted from the data. (c) The Fourier transform of (b). (d) The electron population of Bi_2Se_3 measured at 510 fs delay at 0.54 mJ/cm^2. The arrows show different $\mathbf{k}_{||}$ regions we sample for the SS. (e) Modulation of Bi_2Se_3 SS at 0.54 mJ/cm^2, sampled at different $\mathbf{k}_{||}$ regions. An incoherent background is subtracted off from the data as in (b). (f) The Fourier transform of (e). (g) Bi_2Te_3 $A_{1g}^{(1)}$ phonon-induced energy modulation amplitude as a function of $A_{1g}^{(2)}$ frequency. The slopes of the linear fits across $\mathbf{k}_{||}$ points do not vary much, which justifies averaging over a large region of interest in $\mathbf{k}_{||}$ space to improve the signal-to-noise ratio. The inset contains part of Fig. 4(c), with additional crosses representing the $A_{1g}^{(1)}$ DPs calculated for individual $\mathbf{k}_{||}$ points. (h) Bi_2Te_3 $A_{1g}^{(2)}$ phonon-induced energy modulation amplitude as a function of $A_{1g}^{(2)}$ frequency. Crosses in the inset represent the $A_{1g}^{(2)}$ DPs calculated for individual $\mathbf{k}_{||}$ points.

extraction and leading to higher variations in DPs. Overall, averaging over a larger portion of **k** space to improve the signal-to-noise ratio is justified.

APPENDIX C: COMPLETE DEFORMATION POTENTIAL CALCULATION

As in the main text, we present the simulation details for DP calculations in Bi_2Te_3 first, before we do so for Bi_2Se_3. We show the simulated carrier density $n(z,t)$ and the phonon field $u(z,t)$ in Fig. 8, for both the thin film used in XRD and the bulk sample used in ARPES. This simulation is used to obtain the scaling factors in Eqs. (3) and (10).

We show the measured fluence dependence of the mode frequencies f_i in Fig. 9(a), for different samples and experimental conditions. The large change of the Bi_2Te_3 $A_{1g}^{(2)}$ frequency with increasing fluence shows that f_i can be a good proxy for the absorbed pump energy density. Thus, we can use Eq. (11) to correct for the fluence uncertainty in different experiments.

The DPs are proportional to $[(d\tilde{u}_{SS}/d\tilde{f}_{SS})/(d\tilde{u}_{XRD}/d\tilde{f}_{XRD})]^{-1}$, and hence

$$\left[\frac{(d\tilde{u}_{SS}/d\tilde{f}_{SS})}{(d\tilde{u}_{XRD}/d\tilde{f}_{XRD})}\right]^{-1} = \left(\frac{\tilde{u}_{SS}}{\tilde{u}_{XRD}}\right)^{-1} \frac{(d\tilde{f}_{SS}/dF)}{(d\tilde{f}_{XRD}/dF)}. \quad \text{(C1)}$$

The first factor in Eq. (C1) right-hand side is presented in the main text, assuming a fixed fluence. Simulated fluence (F) dependence of $\tilde{f}_i$ in XRD (using thin film) and ARPES (using bulk) is shown in Fig. 9(b). $\tilde{f}_i$ is obtained from $\tilde{u}_i(t)$ as shown in Fig. 8 by LPSVD. The slopes of linear fits in Fig. 9(b) reproduce the experimental observation that the f_i softening for XRD is larger than ARPES. We use this to calculate the quantity $(d\tilde{f}_{SS}/dF)/(d\tilde{f}_{XRD}/dF)$, the second term of Eq. (C1) right-hand side. It might seem counterintuitive that for a given fluence, the phonon softening is larger in an XRD measurement while the phonon amplitude is larger in an ARPES measurement. This is because phonon amplitudes are quantified by their instantaneous behavior near $t = 0$. Diffusion effects are limited to the timescale of phonon generation of approximately one phonon period. In contrast, the analysis of phonon frequencies requires multiple phonon cycles. This allows for diffusion to act longer, which leads to the larger carrier density in a thin film sample as compared to the surface area of a bulk.

To clearly show the correction factor $[(d\tilde{u}_{SS}/d\tilde{f}_{SS})/(d\tilde{u}_{XRD}/d\tilde{f}_{XRD})]^{-1}$, we plot the simulated, normalized A_{1g} amplitudes as a function of $A_{1g}^{(2)}$ redshift in Fig. 9(c). The slopes are directly used to calculate the quantity $(d\tilde{u}_{SS}/d\tilde{f}_{SS})/(d\tilde{u}_{XRD}/d\tilde{f}_{XRD})$. The slope of the ARPES measurement $(d\tilde{u}_{SS}/d\tilde{f}_{SS})$ is a factor of 2.8 (3.0) larger

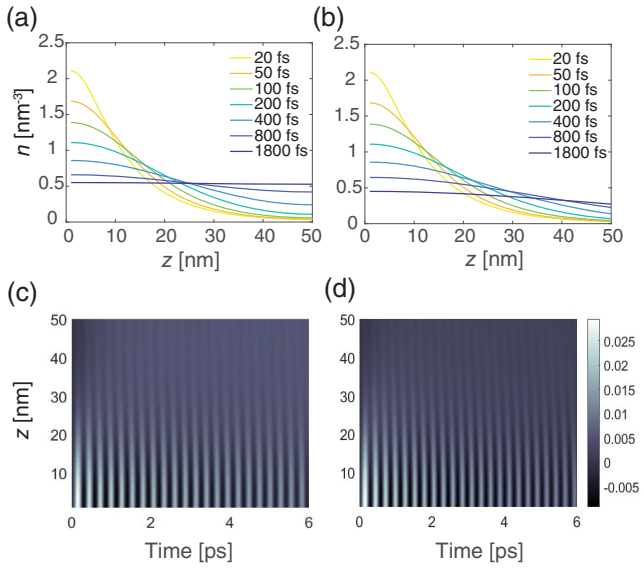

FIG. 8. Diffusivity simulation. Nonequilibrium carrier density profile for different time delays after the laser pump of fluence 2 mJ/cm², in a 50 nm thin film (a) and bulk (b). Coherent phonon field induced by the population of nonequilibrium carriers, in a 50 nm thin film (c) which corresponds to (a), and bulk (d) which corresponds to (b).

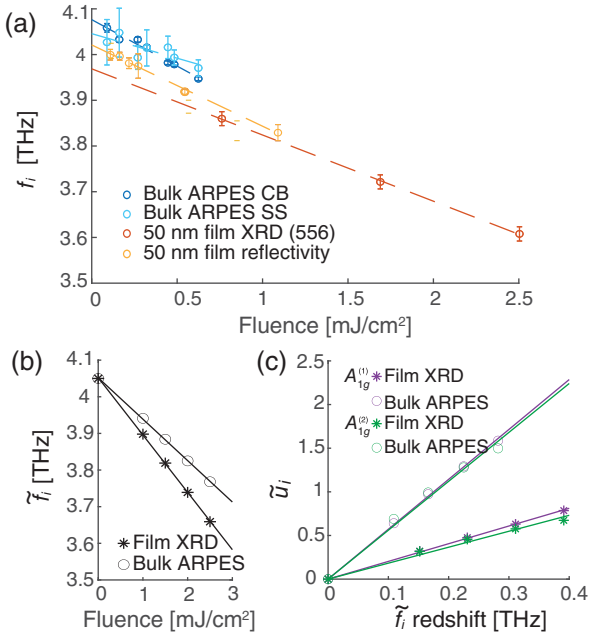

FIG. 9. (a) Linear fluence dependence of the Bi_2Te_3 $A_{1g}^{(2)}$ mode frequency. We include data taken with XRD (50 nm film), ARPES (bulk) and pump-probe optical reflectivity (50 nm film), which span different ranges of absorbed fluences and thus different ranges of f_i. (b) Simulated $A_{1g}^{(2)}$ mode frequency dependence on fluence. (c) Simulated A_{1g} normalized signals of time-resolved ARPES of a bulk sample, and the normalized signals of time-resolved XRD for a 50 nm thin film sample used in the LCLS experiment as a function of $A_{1g}^{(2)}$ frequency redshift.

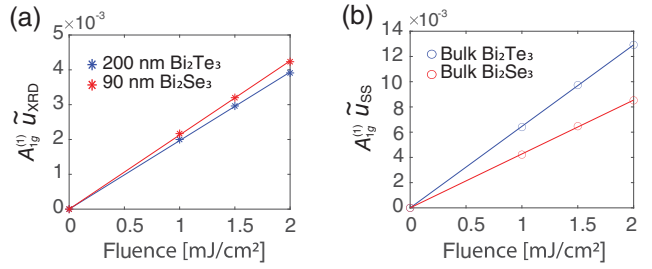

FIG. 10. (a) Simulated time-resolved XRD signal of the $A_{1g}^{(1)}$ response for Bi_2Te_3 film (200 nm) and Bi_2Se_3 film (90 nm), which correspond to the data taken at SACLA. (b) Simulated time-resolved ARPES signal of the $A_{1g}^{(1)}$ response for Bi_2Te_3 bulk and Bi_2Se_3 bulk.

than the XRD measurement $(d\tilde{u}_{\mathrm{XRD}}/d\tilde{f}_{\mathrm{XRD}})$ for the $A_{1g}^{(1)}$ $(A_{1g}^{(2)})$ mode.

Next we consider the carrier diffusion simulation for the DP calculation of Bi_2Se_3. Here, different samples are measured using the same experimental conditions and we can ignore the systematic errors induced by fluence calibration. In these simulations the absolute values of $\tilde{u}$ are irrelevant; only the ratios between them matter. Figure 10 shows that given the same absorbed fluence, the response of Bi_2Te_3 and Bi_2Se_3 differs, both for XRD in Fig. 10(a) and for ARPES in Fig. 10(b). Again, this is due to the difference in carrier diffusivities of Bi_2Te_3 and Bi_2Se_3.

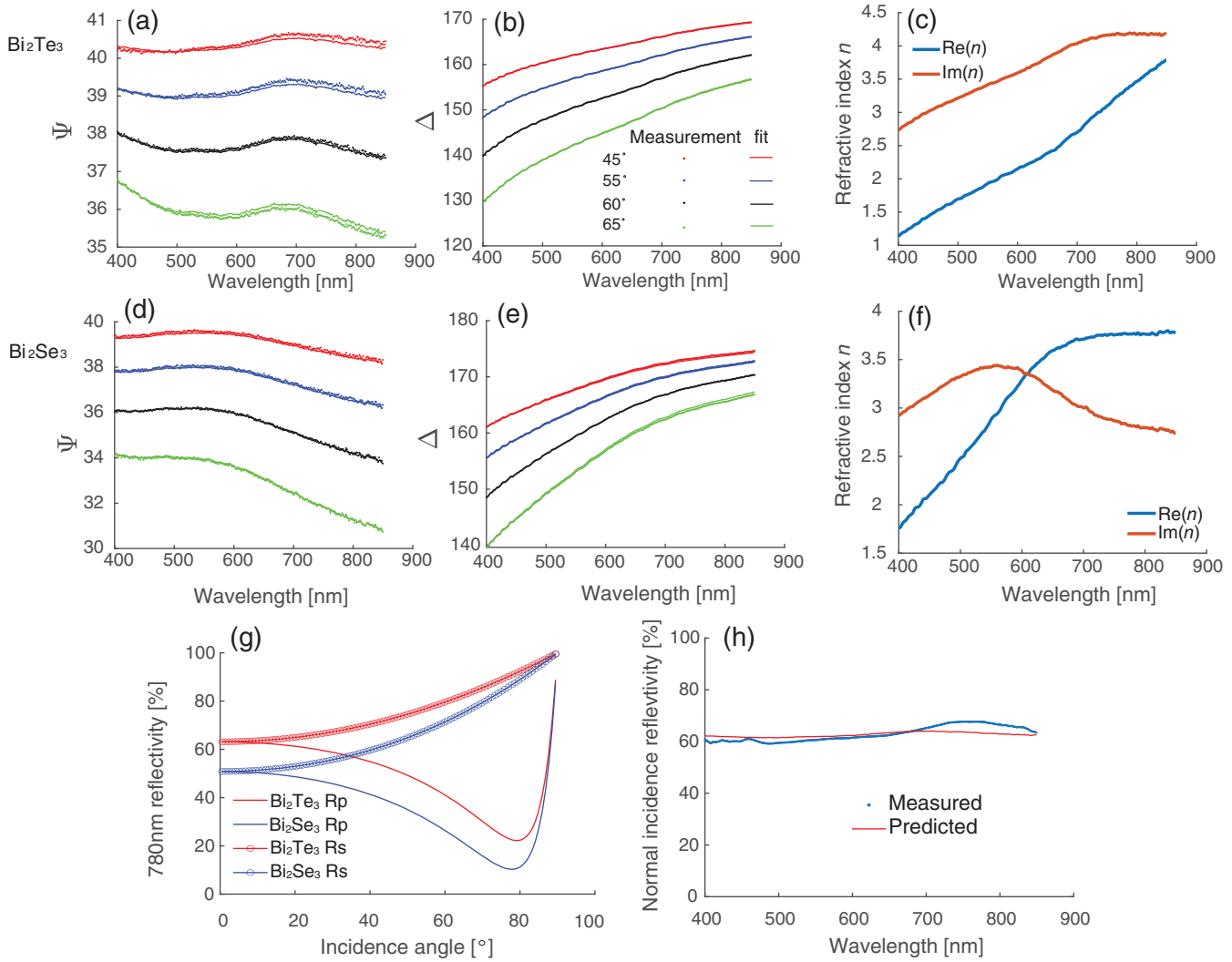

FIG. 11. Ellipsometry data for Bi_2Te_3 and Bi_2Se_3. Panels (a) and (b) show Ψ and Δ from measurement (dots) and fit result (solid curve) for Bi_2Te_3. The reflectivity measurement was conducted at four different incidence angles. The fit uses a multilayer reflection model and takes into account the thickness of film and the refractive index of the substrate. The complex refractive index is shown in (c). (d)–(f) Bi_2Se_3 ellipsometry results. (g) The *s* and *p* reflectivity of 780 nm light as a function of incidence angle. Panel (h) shows the reflectivity of a 250-nm-thick Bi_2Te_3 measured at normal incidence and the predicted reflectivity.

APPENDIX D: ELLIPSOMETRY

We measured ellipsometry data to obtain the complex refractive index and in turn calculate the absorbed fluence in the Bi_2Te_3 and Bi_2Se_3 samples. Ellipsometry measures reflectivity with phase of p and s polarized light. The ratio of them, a complex number, is expressed as $(r_p/r_s) = \tan\Psi e^{i\Delta}$. In Fig. 11 we plot Ψ and Δ as measured (dots) and as fitted (solid curve). Ellipsometry was conducted at four different incidence angles. The fit uses a multilayer reflection model and takes into account the thickness of the film as well as the refractive index of the substrate. The complex refractive indices as fit results are shown in Figs. 11(e) and 11(f). To compare the pump energy density in different measurements using different incidence angles (XRD, 89.5°; ARPES, 50°; optical, <5°; grazing angle is defined as the angle between the beam and the sample normal), we calculate the reflectivity as a function of incidence angle in Fig. 11(g), at a center wavelength of the pump laser of 780 nm. In Fig. 11(h) we show the reflectivity of a 250-nm-thick Bi_2Te_3 measured at normal incidence and the reflectivity predicted from the measured refractive indices, showing good agreement.

APPENDIX E: DFT METHODS

DFT calculations are performed in the local-density approximation (LDA) [68] employing the Hartwigsen-Goedecker-Hutter norm-conserving pseudopotentials [69] using the ABINIT code [70,71]. Spin-orbit coupling is included in all calculations. For electronic band structure calculations, Brillouin zone integrations are performed on a $12 \times 12 \times 1$ Monkhorst-Pack $\mathbf{k}$-points mesh in the slab calculations and $8 \times 8 \times 8$ mesh in the bulk calculations. An energy cutoff for the plane waves of 15 Ha is used. For bulk phonon calculations using density functional perturbation theory, $12 \times 12 \times 12$ and $6 \times 6 \times 6$ $\mathbf{k}$-points and $\mathbf{q}$-points Monkhorst-Pack meshes are used to sample electronic and vibrational states, respectively. We use bulk phonons in all our calculations since they accurately represent the zone center A_{1g} phonons in a slab with many quintuple layers.

In the bulk DFT calculations, we use the experimental lattice parameters given in Table III. In the slab calculations, we fully relax the atomic positions along the [111] direction, i.e., direction perpendicular to the surface, while keeping the in-plane lattice parameters at experimental values. We used 6-QL and 5-QL slabs for Bi_2Te_3 and Bi_2Se_3, respectively, to make sure that the energy gap between the surface states caused by the interaction between the two surfaces is smaller than a meV.

We calculate the forces in photoexcited bulk Bi_2Te_3 and Bi_2Se_3 immediately after photoexcitation using CDFT [73], assuming that n valence electrons are promoted to the conduction band. In CDFT calculation we assume one chemical potential; i.e., electron and hole populations thermalize rapidly according to Fermi-Dirac distribution. For the photoexcited system, with electron-hole carrier density n, we obtain atomic forces F_i in the z or [111] direction on each atom i in the unit cell as

$$F_i(n) = F_i^0(n) + \sum_{j=1}^{5} [z_j - z_j^0]\Phi_{ij}(n). \tag{E1}$$

The interatomic force matrix $\Phi_{ij}(n)$ depends on the carrier density and gives the phonon frequencies $\omega_\lambda(n)$ in the photoexcited system. The atomic forces $F_i^0(n)$ are the forces obtained in the photoexcited system for the equilibrium atomic positions z_j^0 in the ground state. The equilibrium atomic positions of the photoexcited system depend on n and can be found from

$$z_i^{\text{equil}}(n) = z_i^0 - \sum_{j=1}^{5} \Phi_{ij}^{-1}(n) F_j^0(n). \tag{E2}$$

TABLE III. Bi_2Te_3 and Bi_2Se_3 lattice parameters taken from Ref. [72]. a and c are the hexagonal lattice constants, and δ_1 and δ_2 are the internal parameters describing the position of the atoms inside the unit cell.

	a	c	δ_1	δ_2
Bi_2Te_3	4.386 Å	30.497 Å	0.2095	0.4000
Bi_2Se_3	4.143 Å	28.636 Å	0.2117	0.4008

Figure 12 shows key results of the CDFT simulations. The atoms upon photoexcitation shift toward coordinates of higher symmetry (i.e., fractional coordinates move toward integer multiples of 1/5), which is consistent with the experimental observation of atomic motion direction deduced from the diffraction intensity change. The

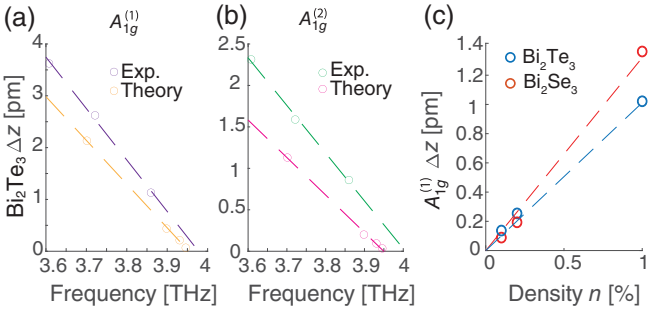

FIG. 12. (a) The constrained DFT simulations of photoexcited bulk Bi_2Te_3 atomic displacements for $A_{1g}^{(1)}$ as a function of the $A_{1g}^{(2)}$ frequency. (b) Same as (a) but for $A_{1g}^{(2)}$ mode atomic displacements. (b) CDFT simulation shows that Bi_2Te_3 and Bi_2Se_3 are driven at similar amplitudes given the same excitation density.

simulations reproduce the atomic motion amplitude of A_{1g} modes as a function of the $A_{1g}^{(2)}$ frequency shift. They also correctly predict that Bi_2Te_3 and Bi_2Se_3 are driven at similar amplitudes given the same excitation density, consistent with the experimental results in Fig. 2(b).

[1] Dong-Xia Qu, Yew San Hor, Jun Xiong, Robert Joseph Cava, and Nai Phuan Ong, *Quantum oscillations and Hall anomaly of surface states in the topological insulator* Bi_2Te_3, Science **329**, 821 (2010).

[2] James G. Analytis, Ross D. McDonald, Scott C. Riggs, Jiun-Haw Chu, G. S. Boebinger, and Ian R. Fisher, *Two-dimensional surface state in the quantum limit of a topological insulator*, Nat. Phys. **6**, 960 (2010).

[3] Faxian Xiu, Liang He, Yong Wang, Lina Cheng, Li-Te Chang, Murong Lang, Guan Huang, Xufeng Kou, Yi Zhou, Xiaowei Jiang *et al.*, *Manipulating surface states in topological insulator nanoribbons*, Nat. Nanotechnol. **6**, 216 (2011).

[4] Bacel Hamdou, Johannes Gooth, August Dorn, Eckhard Pippel, and Kornelius Nielsch, *Surface state dominated transport in topological insulator* Bi_2Te_3 *nanowires*, Appl. Phys. Lett. **103**, 193107 (2013).

[5] Katharina Hoefer, Christoph Becker, Diana Rata, Jesse Swanson, Peter Thalmeier, and Liu Hao Tjeng, *Intrinsic conduction through topological surface states of insulating* Bi_2Te_3 *epitaxial thin films*, Proc. Natl. Acad. Sci. U.S.A. **111**, 14979 (2014).

[6] Richard C. Hatch, Marco Bianchi, Dandan Guan, Shining Bao, Jianli Mi, Bo Brummerstedt Iversen, Louis Nilsson, Liv Hornekær, and Philip Hofmann, *Stability of the* $Bi_2Se_3(111)$ *topological state: Electron-phonon and electron-defect scattering*, Phys. Rev. B **83**, 241303(R) (2011).

[7] Takeshi Kondo, Y. Nakashima, Y. Ota, Y. Ishida, W. Malaeb, K. Okazaki, S. Shin, M. Kriener, Satoshi Sasaki, Kouji Segawa *et al.*, *Anomalous dressing of Dirac fermions in the topological surface state of* Bi_2Se_3, Bi_2Te_3, *and* Cu-*doped* Bi_2Se_3, Phys. Rev. Lett. **110**, 217601 (2013).

[8] Chaoyu Chen, Zhuojin Xie, Ya Feng, Hemian Yi, Aiji Liang, Shaolong He, Daixiang Mou, Junfeng He, Yingying Peng, Xu Liu *et al.*, *Tunable Dirac fermion dynamics in topological insulators*, Sci. Rep. **3**, 1 (2013).

[9] Z.-H. Pan, A. V. Fedorov, D. Gardner, Y. S. Lee, S. Chu, and T. Valla, *Measurement of an exceptionally weak electron-phonon coupling on the surface of the topological insulator* Bi_2Se_3 *using angle-resolved photoemission spectroscopy*, Phys. Rev. Lett. **108**, 187001 (2012).

[10] Rolf Heid, Irina Yu Sklyadneva, and Evgueni V. Chulkov, *Electron-phonon coupling in topological surface states: The role of polar optical modes*, Sci. Rep. **7**, 1 (2017).

[11] Adrian Ruckhofer, Davide Campi, Martin Bremholm, Philip Hofmann, Giorgio Benedek, Marco Bernasconi, Wolfgang E. Ernst, and Anton Tamtögl, *Terahertz surface modes and electron-phonon coupling on* $Bi_2Se_3(111)$, Phys. Rev. Res. **2**, 023186 (2020).

[12] Anton Tamtögl, Patrick Kraus, Nadav Avidor, Martin Bremholm, Ellen M. J. Hedegaard, Bo B. Iversen, Marco Bianchi, Philip Hofmann, John Ellis, William Allison, Giorgio Benedek, and Wolfgang E. Ernst, *Electron-phonon coupling and surface Debye temperature of* $Bi_2Te_3(111)$ *from helium atom scattering*, Phys. Rev. B **95**, 195401 (2017).

[13] Xuetao Zhu, Luiz Santos, Colin Howard, R. Sankar, F. C. Chou, Claudio Chamon, and Michael El-Batanouny, *Electron-phonon coupling on the surface of the topological insulator* Bi_2Se_3 *determined from surface-phonon dispersion measurements*, Phys. Rev. Lett. **108**, 185501 (2012).

[14] Liang Fu, *Odd-parity topological superconductor with nematic order: Application to* $Cu_xBi_2Se_3$, Phys. Rev. B **90**, 100509(R) (2014).

[15] K. Matano, M. Kriener, K. Segawa, Y. Ando, and Guo-qing Zheng, *Spin-rotation symmetry breaking in the superconducting state of* $Cu_xBi_2Se_3$, Nat. Phys. **12**, 852 (2016).

[16] Tomoya Asaba, B. J. Lawson, Colin Tinsman, Lu Chen, Paul Corbae, Gang Li, Yunsheng Qiu, Yew San Hor, Liang Fu, and Lu Li, *Rotational symmetry breaking in a trigonal superconductor* Nb-*doped* Bi_2Se_3, Phys. Rev. X **7**, 011009 (2017).

[17] Shingo Yonezawa, Kengo Tajiri, Suguru Nakata, Yuki Nagai, Zhiwei Wang, Kouji Segawa, Yoichi Ando, and Yoshiteru Maeno, *Thermodynamic evidence for nematic superconductivity in* $Cu_xBi_2Se_3$, Nat. Phys. **13**, 123 (2017).

[18] Kristin Willa, Roland Willa, Kok Wee Song, G. D. Gu, John A. Schneeloch, Ruidan Zhong, Alexei E. Koshelev, Wai-Kwong Kwok, and Ulrich Welp, *Nanocalorimetric evidence for nematic superconductivity in the doped topological insulator* $Sr_{0.1}Bi_2Se_3$, Phys. Rev. B **98**, 184509 (2018).

[19] Jinghui Wang, Kejing Ran, Shichao Li, Zhen Ma, Song Bao, Zhengwei Cai, Youtian Zhang, Kenji Nakajima, Seiko Ohira-Kawamura, P Čermák *et al.*, *Evidence for singular-phonon-induced nematic superconductivity in a topological superconductor candidate* $Sr_{0.1}Bi_2Se_3$, Nat. Commun. **10**, 1 (2019).

[20] Leiqiang Li, Jiang Zeng, Wei Qin, Ping Cui, and Zhenyu Zhang, *Tuning the hydrogen activation reactivity on topological insulator heterostructures*, Nano Energy **58**, 40 (2019).

[21] Jianping Xiao, Liangzhi Kou, Chi Yung Yam, Thomas Frauenheim, and Binghai Yan, *Toward rational design of catalysts supported on a topological insulator substrate*, ACS Catal. **5**, 7063 (2015).

[22] Geert Jan Kroes, *Frontiers in surface scattering simulations*, Science **321**, 794 (2008).

[23] Yoshinori Tokura, *Photoinduced phase transition: A tool for generating a hidden state of matter*, J. Phys. Soc. Jpn. **75**, 011001 (2006).

[24] D. N. Basov, R. D. Averitt, and D. Hsieh, *Towards properties on demand in quantum materials*, Nat. Mater. **16**, 1077 (2017).

[25] Liang Luo, Xu Yang, X. Liu, Zhiyan Liu, Chirag Vaswani, Di Cheng, M. Mootz, Xin Zhao, Yongxin Yao, C.-Z. Wang *et al.*, *Ultrafast manipulation of topologically enhanced surface transport driven by mid-infrared and terahertz pulses in* Bi_2Se_3, Nat. Commun. **10**, 1 (2019).

[26] Edbert J. Sie, Clara M. Nyby, C. D. Pemmaraju, Su Ji Park, Xiaozhe Shen, Jie Yang, Matthias C. Hoffmann, B. K. Ofori-Okai, Renkai Li, Alexander H. Reid *et al.*, *An ultrafast symmetry switch in a Weyl semimetal*, Nature (London) **565**, 61 (2019).

[27] C. Vaswani, L.-L. Wang, D. H. Mudiyanselage, Q. Li, P. M. Lozano, G. D. Gu, D. Cheng, B. Song, L. Luo, R. H. J. Kim, C. Huang, Z. Liu, M. Mootz, I. E. Perakis, Y. Yao, K. M. Ho, and J. Wang, *Light-driven Raman coherence as a nonthermal route to ultrafast topology switching in a Dirac semimetal*, Phys. Rev. X **10**, 021013 (2020).

[28] Niraj Aryal, Xilian Jin, Q. Li, A. M. Tsvelik, and Weiguo Yin, *Topological phase transition and phonon-space Dirac topology surfaces in* $ZrTe_5$, Phys. Rev. Lett. **126**, 016401 (2021).

[29] Liang Luo, Di Cheng, Boqun Song, Lin Lin Wang, Chirag Vaswani, P. M. Lozano, G. Gu, Chuankun Huang, Richard H. J. Kim, Zhaoyu Liu, Joong Mok Park, Yongxin Yao, Kaiming Ho, Ilias E. Perakis, Qiang Li, and Jigang Wang, *A light-induced phononic symmetry switch and giant dissipationless topological photocurrent in* $ZrTe_5$, Nat. Mater. **20**, 329 (2021).

[30] J. Bardeen and W. Shockley, *Deformation potentials and mobilities in non-polar crystals*, Phys. Rev. **80**, 72 (1950).

[31] Ph. Hofmann, I. Yu Sklyadneva, E. D. L. Rienks, and E. V. Chulkov, *Electron–phonon coupling at surfaces and interfaces*, New J. Phys. **11**, 125005 (2009).

[32] T. P. Devereaux, T. Cuk, Z.-X. Shen, and N. Nagaosa, *Anisotropic electron-phonon interaction in the cuprates*, Phys. Rev. Lett. **93**, 117004 (2004).

[33] J. J. Lee, F. T. Schmitt, R. G. Moore, S. Johnston, Y. T. Cui, W. Li, M. Yi, Z. K. Liu, M. Hashimoto, Y. Zhang, D. H. Lu, T. P. Devereaux, D. H. Lee, and Z. X. Shen, *Interfacial mode coupling as the origin of the enhancement of Tc in* FeSe *Films on* $SrTiO_3$, Nature (London) **515**, 245 (2014).

[34] Fabio Boschini, Marta Zonno, and Andrea Damascelli, *Time- and angle-resolved photoemission studies of quantum materials*, arXiv:2309.03935 [Rev. Mod. Phys. (to be published)].

[35] Philip B. Allen, *Theory of thermal relaxation of electrons in metals*, Phys. Rev. Lett. **59**, 1460 (1987).

[36] M. Lisowski, P. A. Loukakos, U. Bovensiepen, J. Stähler, C. Gahl, and M. Wolf, *Ultra-fast dynamics of electron thermalization, cooling and transport effects in* Ru(001), Appl. Phys. A **78**, 165 (2004).

[37] L. Perfetti, P. A. Loukakos, M. Lisowski, U. Bovensiepen, H. Eisaki, and M. Wolf, *Ultrafast electron relaxation in superconducting* $Bi_2Sr_2CaCu_2O_{8+\delta}$ *by time-resolved photoelectron spectroscopy*, Phys. Rev. Lett. **99**, 197001 (2007).

[38] MengXing Na, Arthur K. Mills, Fabio Boschini, Matteo Michiardi, Benjamin Nosarzewski, Ryan P. Day, Elia Razzoli, Alexander Sheyerman, Michael Schneider, Giorgio Levy *et al.*, *Direct determination of mode-projected electron-phonon coupling in the time domain*, Science **366**, 1231 (2019).

[39] S.-L. Yang, J. A. Sobota, D. Leuenberger, Y. He, M. Hashimoto, D. H. Lu, H. Eisaki, P. S. Kirchmann, and Z.-X. Shen, *Inequivalence of single-particle and population lifetimes in a cuprate superconductor*, Phys. Rev. Lett. **114**, 247001 (2015).

[40] S.-L. Yang, J. A. Sobota, Y. He, D. Leuenberger, H. Soifer, H. Eisaki, P. S. Kirchmann, and Z.-X. Shen, *Mode-selective coupling of coherent phonons to the Bi2212 electronic band structure*, Phys. Rev. Lett. **122**, 176403 (2019).

[41] Petra Hein, Stephan Jauernik, Hermann Erk, Lexian Yang, Yanpeng Qi, Yan Sun, Claudia Felser, and Michael Bauer, *Mode-resolved reciprocal space mapping of electron-phonon interaction in the Weyl semimetal candidate* Td-WTe_2, Nat. Commun. **11**, 2613 (2020).

[42] Umberto De Giovannini, Hannes Hübener, Shunsuke A. Sato, and Angel Rubio, *Direct measurement of electron-phonon coupling with time-resolved ARPES*, Phys. Rev. Lett. **125**, 136401 (2020).

[43] L. Rettig, S. O. Mariager, A. Ferrer, S. Grübel, J. A. Johnson, J. Rittmann, T. Wolf, S. L. Johnson, G. Ingold, P. Beaud, and U. Staub, *Ultrafast structural dynamics of the* Fe-*pnictide parent compound* $BaFe_2As_2$, Phys. Rev. Lett. **114**, 067402 (2015).

[44] S. Gerber, S.-L. Yang, D. Zhu, H. Soifer, J. A. Sobota, S. Rebec, J. J. Lee, T. Jia, B. Moritz, C. Jia *et al.*, *Femtosecond electron-phonon lock-in by photoemission and x-ray free-electron laser*, Science **357**, 71 (2017).

[45] H. J. Zeiger, J. Vidal, T. K. Cheng, E. P. Ippen, G. Dresselhaus, and M. S. Dresselhaus, *Theory for displacive excitation of coherent phonons*, Phys. Rev. B **45**, 768 (1992).

[46] H. Barkhuijsen, R. de Beer, W. M. M. J. Bovée, and D. van Ormondt, *Retrieval of frequencies, amplitudes, damping factors, and phases from time-domain signals using a linear least-squares procedure*, J. Magn. Reson. **61**, 465 (1985).

[47] Jens J. Led and Henrik Gesmar, *Application of the linear prediction method to NMR spectroscopy*, Chem. Rev. **91**, 1413 (1991).

[48] Yijing Huang, Shan Yang, Samuel Teitelbaum, Gilberto De la Peña, Takahiro Sato, Matthieu Chollet, Diling Zhu, Jennifer L. Niedziela, Dipanshu Bansal, Andrew F. May, Aaron M. Lindenberg, Olivier Delaire, David A. Reis, and Mariano Trigo, *Observation of a novel lattice instability in ultrafast photoexcited* SnSe, Phys. Rev. X **12**, 011029 (2022).

[49] H. Xiong, J. A. Sobota, S.-L. Yang, H. Soifer, A. Gauthier, M.-H. Lu, Y.-Y. Lv, S.-H. Yao, D. Lu, M. Hashimoto, P. S. Kirchmann, Y.-F. Chen, and Z.-X. Shen, *Three-dimensional nature of the band structure of* $ZrTe_5$ *measured by high-momentum-resolution photoemission spectroscopy*, Phys. Rev. B **95**, 195119 (2017).

[50] J. A. Sobota, S.-L. Yang, D. Leuenberger, A. F. Kemper, J. G. Analytis, I. R. Fisher, P. S. Kirchmann, T. P. Devereaux, and Z.-X. Shen, *Distinguishing bulk and surface electron-phonon coupling in the topological insulator*, Phys. Rev. Lett. **113**, 157401 (2014).

[51] Jonathan A. Sobota, Samuel W. Teitelbaum, Yijing Huang, José D. Querales-Flores, Robert Power, Meabh Allen, Costel R. Rotundu, Trevor P. Bailey, Ctirad Uher, Tom Henighan *et al.*, *Influence of local symmetry on lattice dynamics coupled to topological surface states*, Phys. Rev. B **107**, 014305 (2023).

[52] Anna Pertsova and Carlo M. Canali, *Probing the wavefunction of the surface states in* Bi_2Se_3 *topological*

insulator: A realistic tight-binding approach, New J. Phys. **16**, 063022 (2014).

[53] Hyung-Wook Jeon, Heon-Phil Ha, Dow-Bin Hyun, and Jae-Dong Shim, *Electrical and thermoelectrical properties of undoped* Bi_2Te_3-Sb_2Te_3 *and* Bi_2Te_3-Sb_2Te_3-Sb_2Se_3 *single crystals*, J. Phys. Chem. Solids **52**, 579 (1991).

[54] Yu-Miin Sheu, Y. J. Chien, C. Uher, S. Fahy, and D. A. Reis, *Free-carrier relaxation and lattice heating in photoexcited bismuth*, Phys. Rev. B **87**, 075429 (2013).

[55] Davide Boschetto, Eugene G. Gamaly, Andrei V. Rode, B. Luther-Davies, D. Glijer, T. Garl, O. Albert, Antoine Rousse, and Jean Etchepare, *Small atomic displacements recorded in bismuth by the optical reflectivity of femtosecond laser-pulse excitations*, Phys. Rev. Lett. **100**, 027404 (2008).

[56] Alexander Q. Wu and Xianfan Xu, *Coupling of ultrafast laser energy to coherent phonons in bismuth*, Appl. Phys. Lett. **90**, 251111 (2007).

[57] O. V. Misochko, Muneaki Hase, K. Ishioka, and M. Kitajima, *Observation of an amplitude collapse and revival of chirped coherent phonons in bismuth*, Phys. Rev. Lett. **92**, 197401 (2004).

[58] M. F. DeCamp, D. A. Reis, P. H. Bucksbaum, and R. Merlin, *Dynamics and coherent control of high-amplitude optical phonons in bismuth*, Phys. Rev. B **64**, 092301 (2001).

[59] R. Merlin, *Generating coherent THz phonons with light pulses*, Solid State Commun. **102**, 207 (1997).

[60] C. B. Satterthwaite and R. W. Ure, *Electrical and thermal properties of* Bi_2Te_3, Phys. Rev. **108**, 1164 (1957).

[61] D. H. Auston and C. V. Shank, *Picosecond ellipsometry of transient electron-hole plasmas in germanium*, Phys. Rev. Lett. **32**, 1120 (1974).

[62] Jeff F. Young and H. M. van Driel, *Ambipolar diffusion of high-density electrons and holes in* Ge, Si, *and* GaAs*: Many-body effects*, Phys. Rev. B **26**, 2147 (1982).

[63] P. Janíček, Č. Drašar, L. Beneš, and P. Lošták, *Thermoelectric properties of* Tl*-doped* Bi_2S_3 *single crystals*, Cryst. Res. Technol. **44**, 505 (2009).

[64] Liang Fu, *Hexagonal warping effects in the surface states of the topological insulator* Bi_2Te_3, Phys. Rev. Lett. **103**, 266801 (2009).

[65] E. Golias and J. Sánchez-Barriga, *Observation of antiphase coherent phonons in the warped dirac cone of* Bi_2Te_3, Phys. Rev. B **94**, 161113(R) (2016).

[66] F. Murphy-Armando and S. Fahy, *First-principles calculation of carrier-phonon scattering in n-type* $Si_{1-x}Ge_x$ *alloys*, Phys. Rev. B **78**, 035202 (2008).

[67] Tobias Förster, Peter Krüger, and Michael Rohlfing, *GW calculations for* Bi_2Te_3 *and* Sb_2Te_3 *thin films: Electronic and topological properties*, Phys. Rev. B **93**, 205442 (2016).

[68] J. P. Perdew and Alex Zunger, *Self-interaction correction to density-functional approximations for many-electron systems*, Phys. Rev. B **23**, 5048 (1981).

[69] C. Hartwigsen, S. Goedecker, and J. Hutter, *Relativistic separable dual-space Gaussian pseudopotentials from H to* Rn, Phys. Rev. B **58**, 3641 (1998).

[70] X. Gonze, B. Amadon, P.-M. Anglade, J.-M. Beuken, F. Bottin, P. Boulanger, F. Bruneval, D. Caliste, R. Caracas, M. Côté *et al.*, ABINIT*: First-principles approach to material and nanosystem properties*, Comput. Phys. Commun. **180**, 2582 (2009).

[71] X. Gonze, F. Jollet, F. Abreu Araujo, D. Adams, B. Amadon, T. Applencourt, C. Audouze, J.-M. Beuken, J. Bieder, A. Bokhanchuk *et al.*, *Recent developments in the* ABINIT *software package*, Comput. Phys. Commun. **205**, 106 (2016).

[72] Seizo Nakajima, The crystal structure of $Bi_2Te_{3-x}Se_x$, J. Phys. Chem. Solids **24**, 479 (1963).

[73] É. D. Murray, D. M. Fritz, J. K. Wahlstrand, S. Fahy, and D. A. Reis, *Effect of lattice anharmonicity on high-amplitude phonon dynamics in photoexcited bismuth*, Phys. Rev. B **72**, 060301(R) (2005).